

ROME1-1165/97  
 NDU-HEP-97-EG01  
 February 1997  
 Revised July 1998

## $Z\gamma H$ vertex effects in Higgs production at future $e\gamma$ linear colliders.

E. Gabrielli <sup>a</sup>, V.A. Ilyin <sup>b</sup> and B. Mele <sup>c</sup>.

<sup>a</sup> University of Notre Dame, IN, USA

<sup>b</sup> Institute of Nuclear Physics, Moscow State University, Russia

<sup>c</sup> INFN, Sezione di Roma 1 and Rome University “La Sapienza”, Italy

### Abstract

One-loop production of a Higgs boson in  $e\gamma$  collisions at future accelerators is studied via the process  $e\gamma \rightarrow eH$ , for intermediate Higgs masses. Exact cross sections, including the possibility of longitudinally polarized initial beams, are presented. Confirming previous estimates made in the Weizsäcker-Williams approximation, they are found to be more than two orders of magnitude larger than the cross sections for the crossed process  $e^+e^- \rightarrow H\gamma$ , in the energy range  $\sqrt{s} = (0.5 \div 2)$  TeV. We show that, not only  $e\gamma \rightarrow eH$  has a similar potential as the  $\gamma\gamma \rightarrow H$  process for testing the one-loop  $\gamma\gamma H$  vertex, but, by requiring a final electron tagged at large angle in  $e\gamma \rightarrow eH$ , the  $He$  production provides an excellent way of testing the  $Z\gamma H$  vertex, too. Kinematical distributions for the  $e\gamma \rightarrow eH \rightarrow e(b\bar{b})$  process with a tagged final electron are analyzed, and strategies for controlling the main irreducible background are found. Initial-state-radiation effects are checked to be within a few percent.

e-mail:

egabriel@wave.phys.nd.edu, ilyin@theory.npi.msu.su, mele@roma1.infn.it

# 1 Introduction

The Higgs boson sector is a crucial part of the Standard Model still escaping direct experimental verification. Presently, we know that  $m_H \gtrsim 65\text{GeV}$  [1]. Once the Higgs boson will be discovered either at LEP2 or at LHC, testing the Higgs boson properties will be a central issue at future linear colliders. In particular, an  $e^+e^-$  collider with centre-of-mass (c.m.) energy  $\sqrt{s} \simeq (300 \div 2000)\text{GeV}$  and integrated luminosity  $\mathcal{O}(100)\text{fb}^{-1}$  will allow an accurate determination of the mass, couplings and parity properties of the Higgs particle [2, 3]. Two further options are presently considered for a high-energy linear collider, where one or both the initial  $e^+/e^-$  beams are replaced by photon beams induced by Compton backscattering of laser light on the high-energy electron beams [4]. Then, one can study high-energy electron-photon and photon-photon collisions, where the initial photons are real, to a good degree monochromatic, and have energy and luminosity comparable to the ones of the parent electron beam [5].

In this paper, we analyse the Higgs production in  $e\gamma$  collisions through the process  $e\gamma \rightarrow eH$ . This channel will turn out to be an excellent mean to test both the  $\gamma\gamma H$  and  $Z\gamma H$  one-loop couplings with high statistics. Possible ways to test the couplings  $ggH$ ,  $\gamma\gamma H$  and  $Z\gamma H$  have been extensively studied in the literature. These one-loop vertices, because of the nondecoupling properties of the Higgs boson, are sensitive to the contribution of new particles circulating in the loops, even in the limit  $M_{new} \gg m_H$  [6].

While the  $ggH$  vertex [7] can be tested by the Higgs production via gluon-gluon fusion at LHC, a measurement of the  $\gamma\gamma H$  and  $Z\gamma H$  couplings should be possible by the determination of the BR's for the decays  $H \rightarrow \gamma\gamma$  [8, 9] and  $H \rightarrow \gamma Z$  [10, 9] (see also [11]), respectively. The latter statement holds only for an intermediate-mass Higgs boson (i.e., for  $90\text{GeV} \lesssim m_H \lesssim 140\text{GeV}$ ), where both  $\text{BR}(H \rightarrow \gamma\gamma)$  and  $\text{BR}(H \rightarrow \gamma Z)$  reach their maximum values, which is  $\mathcal{O}(10^{-3})$ .

Another promising way of measuring the  $\gamma\gamma H$  coupling for an intermediate-mass Higgs boson will be realized through Higgs production in  $\gamma\gamma$  collisions [12, 13]. To this end, the capability of tuning the  $\gamma\gamma$  c.m. energy on the Higgs mass, through a good degree of the photons monochromaticity, will be crucial for not diluting too much the  $\gamma\gamma \rightarrow H$  resonant cross section over the c.m. energy spectrum.

The process  $e\gamma \rightarrow eH$ , that we consider here, offers a further interesting way of testing both the  $\gamma\gamma H$  and  $Z\gamma H$  Higgs vertices. Indeed, we will show that, while the  $\gamma$ -exchange  $\gamma\gamma H$  contribution is dominant in the total cross section, by requiring a large transverse momentum of the final electron (or Higgs boson), one enhances the  $Z$ -exchange  $Z\gamma H$  contribution, while keeping the corresponding rate still to an observable level. The further contribution given by the box diagrams with  $W$  and  $Z$  exchange survives at large angles too, but is relatively less important. Furthermore, while the  $\gamma\gamma H$  and  $Z\gamma H$  channels increase logarithmically with the c.m. collision energy, the contribution from boxes starts decreasing at  $\sqrt{s} \gtrsim 400\text{GeV}$ .

A further advantage of the  $e\gamma \rightarrow eH$  process with respect to the resonant  $\gamma\gamma \rightarrow H$  pro-

duction is that the former is much less crucially dependent on the tuning of the c.m. collision energy to  $m_H$ . As a consequence, although the resonant cross section  $\sigma_{res}(\gamma\gamma \rightarrow H)$  is in general much larger than  $\sigma(e\gamma \rightarrow eH)$ , the effect of the  $\gamma$ -spectrum smearing can make the two rates of the same order of magnitude (see also [13]).

The cross section for the process  $e\gamma \rightarrow eH$  has previously been studied in the Weizsäcker-Williams (WW) approximation [14], where the only channel contributing is the (almost real)  $\gamma$ -exchange in the  $t$ -channel, induced by the  $\gamma\gamma H$  vertex [15] (see also [16], where the pseudoscalar Higgs-boson production is considered). Although, as we will see, this method provides a rather good estimate of the  $e\gamma \rightarrow eH$  total cross sections, it is unable to assess the importance of the  $Z\gamma H$  (and box) effects. This we will address particularly in our exact treatment of  $e\gamma \rightarrow eH$ .

Although, cross sections for the process  $e\gamma \rightarrow eH$  are quite large also for heavy Higgs bosons (e.g.,  $\sigma(m_H \simeq 400\text{GeV}) > 1\text{ fb}$  for  $\sqrt{s} \gtrsim 500\text{ GeV}$ ), we will concentrate on the intermediate Higgs mass case. Hence, we will carry out a detailed analysis of the main background, assuming that the decay  $H \rightarrow b\bar{b}$  is dominant.

In principle, the same physics could be tested in the crossed process,  $e^+e^- \rightarrow H\gamma$ , which has been widely studied [17, 18, 19]. Unfortunately, the  $e^+e^- \rightarrow H\gamma$  channel suffers from small rates, which are further depleted at large energies by the  $1/s$  behavior of the dominant s-channel diagrams. Also, in this case, it is more difficult to separate the  $Z\gamma H$  contribution on the basis of kinematical distributions. As a consequence, if a  $e\gamma$  option of the linear collider will be realized with similar luminosity of the  $e^+e^-$  option, the  $e\gamma \rightarrow eH$  channel will turn out to be much more interesting than the process  $e^+e^- \rightarrow H\gamma$ , for finding possible deviations from the standard-model one-loop Higgs vertices.

The plan of the paper is the following. In Section 2, we present the analytical results for the complete helicity amplitudes of the  $e\gamma \rightarrow eH$  process. In Section 3, numerical results for the exact total cross section are given and compared to the ones corresponding to the tree-level Higgs production in  $e\gamma \rightarrow H\nu_e W$ . Also, a discussion of the relative importance of the different one-loop vertices and boxes in  $e\gamma \rightarrow eH$  is presented. In Section 4, the rates for the main background processes are estimated, and strategies for their control are suggested. Initial-beam polarization effects are discussed in Section 5, while, in Section 6, we estimate the influence of the Initial State Radiation (ISR) on the above picture. In Section 7, we discuss the expected precision on a measurement of the  $Z\gamma H$  effects through  $e\gamma \rightarrow eH$ , and point out a possible strategy, based on the angular asymmetry of the final electron, for further optimizing the ratio  $S/B$ . Finally, in Section 8, we draw our conclusions. In the Appendix, we discuss some technical details of the computation.

## 2 Helicity amplitudes

In this section we give the analytical expression for the matrix element of the process

$$e^-(k_1)\gamma(k_2) \rightarrow e^-(k_3)H(k_4) \quad (1)$$

as a function of the initial electron and photon helicities, where  $k_i$  are the particles momenta. We calculate the amplitude in the *'t-Hooft-Feynman gauge* and in the chiral limit approximation for the electron mass.

In the *unitary gauge*, the Feynman diagrams which contribute to this process are given in figures 1–4 (for the figures of the Feynman diagrams, we used the program GRACEFIG created by S. Kawabata). In figures 1 and 2, we show the fermion and  $W$  triangle loop respectively, with both  $\gamma$  and  $Z$  exchange in the  $t$ -channel, where in the fermion loop we consider only the contribution of the top quark. To these diagrams, the corresponding ones with opposite orientation for the fermion and  $W$  loop have to be added. In figures 3 and 4, the  $W$ -box and  $Z$ -box, along with the related  $eeH$  vertex diagrams, are presented, respectively. The  $eeH$  vertex cannot be neglected in the chiral limit, since only the divergent part of this vertex is proportional to the electron mass. Indeed, its finite part is proportional to the momentum square of the off-shell electron, and it is not zero in the chiral limit. Moreover, the finite part of the  $eeH$  vertex is needed for the gauge invariance of the total amplitude.

In the *'t-Hooft-Feynman gauge*, we have to add to the first diagram in figure 2 the one where the  $W$ -lines are substituted by the  $W$ -ghosts. Furthermore, we have to add to the diagrams of figures 2 and 3 the ones where the  $W$ -lines in the loops are substituted by different combinations of  $W$ -boson and  $W$ -goldstone propagators. For example, there are two diagrams associated with the box diagrams in figure 3, where the  $W$  propagator not connected with the electron is substituted by a  $W$ -goldstone propagator. However, starting from the topology of the first two diagrams in figure 2, there are new diagrams to add that cannot be generated by the above rule. The latter contain 4-legs vertices where the photon interacts with a  $W$ -goldstone and a Higgs boson, both in the  $\gamma$  and  $Z$   $t$ -channel. In particular, in the *'t-Hooft-Feynman gauge*, 52 diagrams replace the first two of figure 2: 26 with  $\gamma$ -exchange plus 26 with  $Z$ -exchange in  $t$ -channel. In the following, when we refer to figures 2 and 3, the complete subsets of the corresponding diagrams in the *'t-Hooft-Feynman gauge* are implied.

The third diagram of figure 2 is given by the insertion of the vertex  $Z\gamma H$  proportional to the counterterm coming from the renormalization of the  $Z$ - $\gamma$  mixing self-energy function at the one-loop level. This diagram is necessary to provide the ultra-violet finiteness of the  $W$ -loop contributions. In our calculation, we have used the on-shell renormalization scheme. Hence, explicit contributions from the diagrams with self-energy functions are missing.

The total amplitude for the process (1) is of course QED gauge invariant. This means that, replacing in each diagram the photon polarization vector  $e^\mu(\lambda, k_2)$  by its momentum  $k_2^\mu$  (here and below  $\lambda \equiv P_\gamma = \pm 1$  is the photon helicity), the sum over the whole set of diagrams has

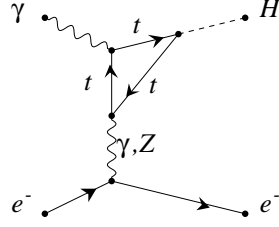


Figure 1: Feynman diagram with fermion triangle loop.

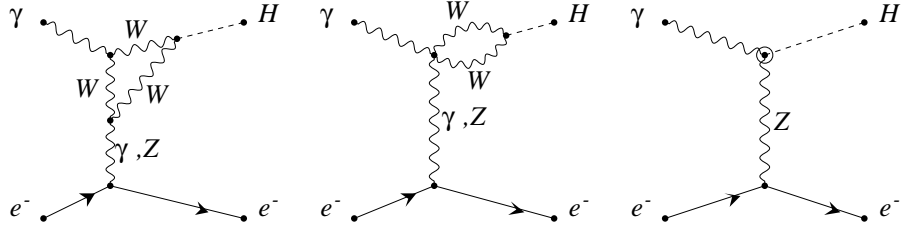


Figure 2: Feynman diagrams with  $W$ -triangle loop.

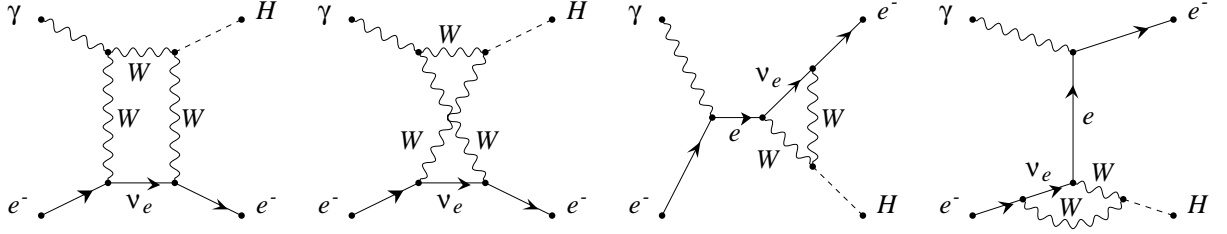


Figure 3: Subset of Feynman diagrams with  $W$ -box loop and related  $eeH$  vertex.

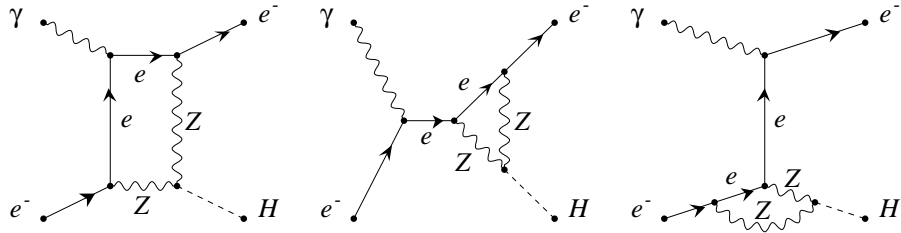


Figure 4: Subset of diagrams with  $Z$ -box loop and related  $eeH$  vertex.

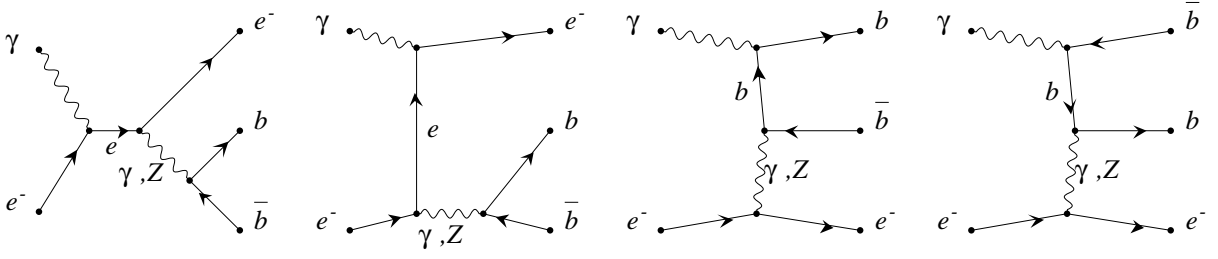


Figure 5: Diagrams for the  $e\gamma \rightarrow ebb\bar{b}$  background.

to vanish. In general, a single diagram (or subset of diagrams) is not transverse in the photon momentum by itself, but we can select the non-transverse part by just taking the terms that do not vanish after this substitution. Then, we find that it is possible to divide the whole set of diagrams into a few QED gauge-invariant subsets of diagrams :

- i) fermion-loops with  $\gamma$  in the  $t$ -channel (figure 1);
- ii) fermion-loops with  $Z$  in the  $t$ -channel (figure 1);
- iii)  $W$  triangle-loops (figure 2) +  $W$  boxes and related  $eeH$  vertices (figure 3);
- iv)  $Z$ -box and related  $eeH$  vertices (figure 4).

Below, we will see that the  $W$ -triangle and  $W$ -box diagrams give rise to QED gauge non-invariant terms that cancel in the sum.

In order to get the analytical expression for the amplitude as a function of the initial particle helicities, we decompose the Feynman amplitude in terms of the so-called *standard matrix elements* defined as

$$\begin{aligned}
 M_1(\sigma, \lambda) &\equiv \bar{u}^\sigma(k_3) \hat{e}(\lambda) u^\sigma(k_1) , \\
 M_2(\sigma, \lambda) &\equiv \bar{u}^\sigma(k_3) \hat{k}_2 u^\sigma(k_1) \cdot (e(\lambda, k_2), k_3) , \\
 M_3(\sigma, \lambda) &\equiv -\bar{u}^\sigma(k_3) \hat{k}_2 u^\sigma(k_1) \cdot (e(\lambda, k_2), k_1) .
 \end{aligned} \tag{2}$$

Here  $u^\sigma(k)$  denotes a spinor state for electrons with helicity  $\sigma/2$  ( $\sigma \equiv P_e = \pm 1$ ) and momentum  $k$  ( $\hat{k} = k^\mu \gamma_\mu$ , where  $\gamma_\mu$  are the Dirac's  $\gamma$ -matrices). Note that these elements contain the complete information about the polarizations of the initial electrons and photons.

The amplitude can be expressed in terms of the standard matrix elements in the center-of-mass system (CMS), where the latter become\*:

$$M_1(\sigma, \lambda) = -\sqrt{-\frac{t}{2}}(1 + \sigma\lambda), \quad M_2(\sigma, \lambda) = \sqrt{-\frac{t}{2}}u, \quad M_3(\sigma, \lambda) = 0 \tag{3}$$

---

\*The same expressions still hold after a Lorentz boost along the collision axis of the process  $e\gamma \rightarrow eH$ .

with the Mandelstam variables defined as:

$$s = (k_1 + k_2)^2, \quad t = (k_1 - k_3)^2, \quad u = (k_2 - k_4)^2. \quad (4)$$

The last equality in (3) is due to the orthogonality in the CMS of the photon polarization vector  $e(\lambda, k_2)$  and the electron momentum  $k_1$ . Nevertheless, we calculate the coefficients of  $M_3$ , too. These coefficients will be useful for the analysis of the QED gauge invariance of the result. Moreover, they will help us to get more compact analytical answers.

The amplitude corresponding to each diagram can be expressed in the following form:

$$M_1(\sigma, \lambda) \cdot \mathcal{B}_1 + M_2(\sigma, \lambda) \cdot \mathcal{B}_2 + M_3(\sigma, \lambda) \cdot \mathcal{B}_3, \quad (5)$$

where the coefficients  $\mathcal{B}_i$  include the loop integrals. The transversality in the photon momentum implies a linear relation between the coefficients  $\mathcal{B}_i$  for the QED gauge-invariant sector of each diagram or subset of diagrams. In fact, after the substitution  $e^\mu \rightarrow k_2^\mu$  in the standard matrix elements (2) and then in (5), we find that, for each QED gauge-invariant subset in the amplitude, these coefficients satisfy the following identity:

$$\mathcal{B}_1 - \frac{u}{2}\mathcal{B}_2 - \frac{s}{2}\mathcal{B}_3 = 0. \quad (6)$$

As a consequence, the partial amplitudes can be represented in the following form, where the standard elements are substituted by their explicit values (3):

$$\frac{1}{2}\sqrt{-\frac{t}{2}} [(u\mathcal{B}_2 - s\mathcal{B}_3) - \sigma\lambda(u\mathcal{B}_2 + s\mathcal{B}_3)]. \quad (7)$$

The final result can be further simplified by using the crossing symmetry connecting the process (1) to the crossed one  $e^+(k_3)\gamma(k_2) \rightarrow e^+(k_1)H(k_4)$ . If we perform a crossing transformation ( $s \leftrightarrow u$ ,  $\sigma \rightarrow -\sigma$ ) in the matrix element of the process (1), we get the same function with opposite electric charge and  $Z$ -charge of the electron, (i.e., with  $Q_e \rightarrow -Q_e$ , and  $g_e \rightarrow -g_e$ ). Of course, for the  $Z$ -charge the change of the electron helicity has to be taken into account, too. We found that, for the QED gauge-invariant component of each subset of the diagrams represented in figures 1–4, this symmetry is fulfilled, what simplifies further our formulas. Indeed, this symmetry implies that the form factor  $u\mathcal{B}_2 - s\mathcal{B}_3$  is antisymmetric with respect to the substitution  $s \leftrightarrow u$ , while  $u\mathcal{B}_2 + s\mathcal{B}_3$  is symmetric (i.e.,  $\mathcal{B}_2 \leftrightarrow \mathcal{B}_3$  for  $s \leftrightarrow u$ ). Then, instead of the coefficients  $\mathcal{B}_2$  and  $\mathcal{B}_3$ , it is worthwhile to consider the following symmetric and antisymmetric combinations:

$$\mathcal{F}^s \equiv \frac{u\mathcal{B}_2 + s\mathcal{B}_3}{2}, \quad \mathcal{F}^a \equiv \frac{u\mathcal{B}_2 - s\mathcal{B}_3}{2}. \quad (8)$$

Using the above form factors, our final analytical results can be represented in the following compact form

$$\sqrt{-\frac{t}{2}} [\mathcal{F}^a - \sigma\lambda\mathcal{F}^s]. \quad (9)$$

Note that all the dependence on the photon helicity is concentrated in the explicit factor of the second term in (9). Hence, when one averages over the photon helicity, the dependence on the electron helicity arises only from the  $Ze\bar{e}$  coupling. Since  $g_e^- \simeq -0.658$  and  $g_e^+ \simeq 0.538$ , the  $Z$   $t$ -channel contributions have opposite signs in the amplitudes for left-handed and right-handed electrons. Moreover, in the region of large transverse momentum, there is a moderate difference between the  $\gamma$  and  $Z$   $t$ -channel propagators. This explains the destructive interference of the  $\gamma$  and  $Z$   $t$ -channels for a right-handed electron beam, and the mutual enhancement of these contributions in the case of left-handed electrons, when the photon beam is unpolarized (see also section 5).

Because of the crossing symmetry for  $s \leftrightarrow u$ , one has  $\mathcal{B}_2 = \mathcal{B}_3$  in eq. (5), for all the triangle amplitudes. This means that, for this class of diagrams, the formula (9) can be further simplified into:

$$\frac{1}{2} \Lambda(\sigma, \lambda) \cdot \mathcal{T} , \quad (10)$$

where  $\mathcal{T} = \mathcal{B}_2 = \mathcal{B}_3$  and

$$\Lambda(\sigma, \lambda) \equiv \sqrt{-\frac{t}{2}} [(u - s) - \sigma\lambda(u + s)] . \quad (11)$$

Finally, the differential cross section for the process with longitudinally polarized photon and electron beams <sup>†</sup> is given by

$$\frac{d\sigma(e\gamma \rightarrow eH)}{d\Omega} = \frac{1 - m_H^2/s}{64\pi^2 s} (\alpha^2 M_Z)^2 |M(\sigma, \lambda)|^2, \quad (12)$$

where  $\Omega$  is the spherical scattering angle of the final electron, and the analytical expression for the total QED gauge-invariant matrix element can be expressed as:

$$\begin{aligned} \mathcal{M}(\sigma, \lambda) = & \mathcal{M}_{\Delta_\gamma^f}(\sigma, \lambda) + \mathcal{M}_{\Delta_Z^f}(\sigma, \lambda) + \mathcal{M}_{\Delta_{\gamma,1}^w}(\sigma, \lambda) + \mathcal{M}_{\Delta_{\gamma,2}^w}(\sigma, \lambda) + \\ & \mathcal{M}_{\Delta_{Z,1}^w}(\sigma, \lambda) + \mathcal{M}_{\Delta_{Z,2}^w}(\sigma, \lambda) + \mathcal{M}_{\Box_w}(\sigma, \lambda) + \mathcal{M}_{\Box_Z}(\sigma, \lambda) . \end{aligned} \quad (13)$$

The partial amplitudes  $\mathcal{M}_i$  are given by the following QED gauge-invariant contributions:

- Triangle fermion loops:

$$\begin{aligned} \mathcal{M}_{\Delta_{(\gamma,Z)}^f}(\sigma, \lambda) = & \frac{m_t^2}{M_Z^2} N_c \frac{Q_t}{s_w c_w} \mathcal{P}_{(\gamma,Z)}^f \cdot \Lambda(\sigma, \lambda) \cdot [\mathcal{T}_1(m_t) - 2\mathcal{T}_2(m_t)] \\ \mathcal{P}_\gamma^f = & \frac{2Q_e Q_t}{-t}, \quad \mathcal{P}_Z^f = \frac{g_e^\sigma(g_t^+ + g_t^-)}{-t + M_Z^2}. \end{aligned} \quad (14)$$

---

<sup>†</sup>Of course, the unpolarized cross section can be obtained by averaging over the helicity of the initial particle(s).



Here,  $\mathcal{M}_{\Delta_\gamma^f}$  and  $\mathcal{M}_{\Delta_Z^f}$  represent the contributions of the  $\gamma$  and  $Z$   $t$ -channel, respectively. In the above formulae,  $N_c = 3$  is the color weight of the  $t$ -quark, while the electric and  $Z$  charges of the fermions,  $Q_f$  and  $g_f^\pm$ , are given by

$$Q_e = -1, \quad g_e^+ = -Q_e \frac{s_w}{c_w}, \quad g_e^- = -\frac{1/2 + Q_e s_w^2}{s_w c_w},$$

$$Q_t = \frac{2}{3}, \quad g_t^+ = -Q_t \frac{s_w}{c_w}, \quad g_t^- = \frac{1/2 - Q_t s_w^2}{s_w c_w}.$$

Also,  $s_w \equiv \sin \theta_W$  and  $c_w \equiv \cos \theta_W$ , with  $\theta_W$  the Weinberg angle.

The expressions for the one-loop form factors  $\mathcal{T}_1(m)$  and  $\mathcal{T}_2(m)$  are given by:

$$\begin{aligned} \mathcal{T}_1(m) &\equiv C_0(m, -k_4, m, k_3 - k_1, m), \\ \mathcal{T}_2(m) &\equiv \frac{1}{s+u} \left\{ 2m^2 \cdot \mathcal{T}_1(m) + \frac{t}{s+u} \cdot [B_0(t, m^2, m^2) - B_0(m_H^2, m^2, m^2)] - 1 \right\} \end{aligned} \quad (15)$$

where the functions  $C_0$  and  $B_0$  are defined in the Appendix<sup>†</sup>. The form factors  $\mathcal{T}_1(m)$  and  $\mathcal{T}_2(m)$  can also be expressed in terms of elementary functions (see [8, 9]).

- Triangle W loops:

$$\begin{aligned} \mathcal{M}_{\Delta_{(\gamma,Z),1}^W}(\sigma, \lambda) &= \frac{m_H^2}{M_Z^2} \frac{1}{s_w c_w} \mathcal{P}_{(\gamma,Z),1}^W \cdot \Lambda(\sigma, \lambda) \cdot [\mathcal{T}_2(M_W)] , \\ \mathcal{P}_{\gamma,1}^W &= \frac{Q_e}{-t}, \quad \mathcal{P}_{Z,1}^W = \frac{g_e^\sigma(1 - 2s_w^2)}{2s_w c_w} \cdot \frac{1}{-t + M_Z^2} , \end{aligned} \quad (16)$$

The terms  $\mathcal{M}_{\Delta_{(\gamma,Z),1}^W}$  include the loop with the  $W$ -goldstone propagators only. Three diagrams contribute both in the photon and  $Z$  exchange. The presence of terms proportional to  $m_H^2/M_Z^2$  is a consequence of the Higgs mechanism and the decoupling of the longitudinal components of the  $W$  boson at high energy.

$$\begin{aligned} \mathcal{M}_{\Delta_{(\gamma,Z),2}^W}(\sigma, \lambda) &= \frac{c_w}{s_w} \mathcal{P}_{(\gamma,Z),2} \cdot \Lambda(\sigma, \lambda) \cdot [-A_1^{(\gamma,Z)} \mathcal{T}_1(M_W) + A_2^{(\gamma,Z)} \mathcal{T}_2(M_W)] , \\ \mathcal{P}_{\gamma,2}^W &= \frac{Q_e}{-t}, \quad A_1^\gamma = 8, \quad A_2^\gamma = 6, \\ \mathcal{P}_{Z,2}^W &= \frac{g_e^\sigma}{-t + M_Z^2}, \quad A_1^Z = 6 \frac{c_w}{s_w} - 2 \frac{s_w}{c_w}, \quad A_2^Z = 5 \frac{c_w}{s_w} - \frac{s_w}{c_w}. \end{aligned} \quad (17)$$

The terms  $\mathcal{M}_{\Delta_{(\gamma,Z),2}^W}$  include the contribution of the  $W$ -triangle diagrams with  $W$ -ghosts and with a mixture of  $W$ -bosons and  $W$ -goldstones running in the loop. In the  $\mathcal{M}_{\Delta_{Z,2}^W}$  term, we also include the diagram with the  $Z\gamma H$  counterterm.

---

<sup>†</sup>Note that, in the limit  $t \rightarrow 0$ , the  $B_0$  integrals do not contribute due to the factor  $t$  in (15). Hence, the  $C_0$  integrals give the dominant contribution to the total cross section.

- $W$  and  $Z$  boxes with related  $eeH$  vertices:

$$\mathcal{M}_{\square_{(W,Z)}}(\sigma, \lambda) = \frac{\mathcal{P}_{(W,Z)}^{\square}}{s_w c_w} \sqrt{-\frac{t}{2}} \cdot [\mathcal{D}_{(W,Z)}^a - \sigma \lambda \mathcal{D}_{(W,Z)}^s], \quad (18)$$

$$\mathcal{P}_W^{\square} = -2 \frac{c_w^2}{s_w^2} \delta_e^{\sigma}, \quad \mathcal{P}_Z^{\square} = 4(g_e^{\sigma})^2 Q_e,$$

where  $\delta_e^+ = 0$ ,  $\delta_e^- = 1$ , and the form factors  $D_{(W,Z)}^{s,a}$  are the symmetric and antisymmetric parts of the functions

$$\begin{aligned} \mathcal{D}_W &\equiv u(D_3^W + D_{23}^W + \tilde{D}_1^W - \tilde{D}_{12}^W - \tilde{D}_{22}^W), \\ \mathcal{D}_Z &\equiv u(D_{12}^Z + D_{22}^Z) \end{aligned} \quad (19)$$

under the crossing  $s \leftrightarrow u$  symmetry transformation. The functions  $D_i^{(W,Z)}$  appearing in eqs. (19) contain the results of the box loop-integrals, and are related to the integrals defined in the Appendix in the following way:

$$D_i^W = D_i(0, k_1, M_W, k_1 + k_2, M_W, k_3, M_W), \quad \tilde{D}_i^W = D_i^W|_{s \leftrightarrow u}, \quad (20)$$

$$D_i^Z = D_i(m_e, k_2, m_e, k_2 - k_3, M_Z, -k_1, M_Z). \quad (21)$$

In the  $Z$ -box functions in eq. (21), we restore the electron mass since the integrals  $D_i$  are not separately finite for  $m_e = 0$ . Of course, the total amplitude has to be insensitive to the value of  $m_e$  used to regularize each singular  $Z$ -box integral. We checked the stability of the total result numerically, for a wide range of  $m_e$ , going from  $10^{-34}$  GeV up to its physical value.

In the following sections, we refer to the different QED gauge-invariant contributions defined above as:

$$\begin{aligned} \text{"}\gamma\gamma H\text{"} &\text{ corresponding to } \mathcal{M}_{\Delta_{\gamma}^f} + \mathcal{M}_{\Delta_{\gamma,1}^W} + \mathcal{M}_{\Delta_{\gamma,2}^W} \\ \text{"}Z\gamma H\text{"} &\text{ corresponding to } \mathcal{M}_{\Delta_Z^f} + \mathcal{M}_{\Delta_{Z,1}^W} + \mathcal{M}_{\Delta_{Z,2}^W} \\ \text{"}BOX\text{"} &\text{ corresponding to } \mathcal{M}_{\square_W} + \mathcal{M}_{\square_Z} \end{aligned}$$

For completeness, we now show the analytical results for the QED gauge non-invariant terms, arising from the  $W$ -triangle and  $W$ -box diagrams. As we checked, the sum of these terms vanishes. They can be worked out by calculating all the coefficients  $\mathcal{B}_i$  and then performing the substitutions  $e(\lambda, k_2) \rightarrow k_2$  in (5). From the  $W$ -triangle diagrams, we obtain for such terms

$$\mathcal{M}_{\Delta_{(\gamma,Z),3}^W}(\sigma, \lambda) = \frac{c_w}{s_w} \mathcal{P}_{(\gamma,Z),3} \cdot [\mathcal{K}_{(\gamma,Z)} \cdot M_1(\sigma, \lambda) \cdot \mathcal{T}_1(M_W)], \quad (22)$$

$$\mathcal{P}_{\gamma,3} = -\frac{Q_e}{-t}, \quad \mathcal{P}_{Z,3} = \frac{c_w g_e^{\sigma}}{s_w} \cdot \frac{1}{-t + M_Z^2}.$$

In eq. (22), the coefficients  $\mathcal{K}_{(\gamma,Z)}$ , arising from the  $W$ -triangle diagrams with  $W$ -ghosts and with a mixture of  $W$ -bosons and  $W$ -goldstones running in the loop, are given by

$$\mathcal{K}_{\gamma} = 3t, \quad \mathcal{K}_Z = 3(-t + M_Z^2), \quad (23)$$

and cancel the corresponding  $\gamma$  and  $Z$  propagators. After summing the two terms in (22), we obtain

$$\mathcal{M}_{\Delta_{(\gamma+Z),3}^W}(\sigma, \lambda) = \frac{c_w \delta_e^\sigma}{2s_w^3} [-3M_1(\sigma, \lambda) \cdot \mathcal{T}_1(M_W)]. \quad (24)$$

This term is exactly cancelled by an opposite term coming from the QED gauge non-invariant contribution of the  $W$ -box diagrams (figure 3).

We stress that the  $eeH$ -vertex diagrams must be added to the  $W$ -box diagrams in order to fulfil the QED gauge-invariance identity (6) for this subset of diagrams, after the cancellation of the term (24). Note that the  $eeH$ -vertex diagrams contribute through the  $\mathcal{B}_1$  coefficients to the weight of the standard matrix element  $M_1$  (2). In the case of the  $Z$ -box diagram (figure 4), the identity (6) is fulfilled automatically when one adds the corresponding  $eeH$  vertex diagrams.

We checked that our expressions for the one-loop form factors agree with that of ref. [17, 18, 19], where the crossed process  $e^+e^- \rightarrow \gamma H$  was investigated. We also checked that our loop form factors  $\mathcal{B}_i$  are in agreement with the corresponding loop form factors for the process  $e^+e^- \rightarrow HZ$  in [20], if the proper crossing transformation is made and the  $Z$  vertices are replaced by the related  $\gamma$  vertices.

Some comments on the gauge dependence of our decomposition in  $\gamma\gamma H$ ,  $Z\gamma H$  and  $BOX$  contributions of eq. (13) are in order. By construction, the identity (6), which is equivalent to the photon transversality, is fulfilled by these contributions separately. One can check that our decomposition corresponds to the  $\gamma\gamma H$ ,  $Z\gamma H$  and  $e^+e^-\gamma H$  Green functions in the so-called non-linear gauge, where the derivative in the 't-Hooft-Feynman gauge for the  $W$  field is replaced by the corresponding covariant derivative. It has been shown [17] that, in this gauge, the Slavnov-Taylor identities for the  $\gamma\gamma H$  and  $Z\gamma H$  Green functions are simply equivalent to the transversality with respect to the photon momenta.

Here, we want to stress, first of all, some technical advantages of the proposed calculation method, based on exploiting the transversality identity (6). Indeed, we chose the widely used 't-Hooft-Feynman gauge, and decomposed the Feynman amplitudes in terms of a set of standard matrix elements. We used the set (2), although this choice is not unique. Then, using the transversality of the physical amplitudes, we found that the coefficients of the standard matrix elements have to fulfill some linear identity, that in our case is eq. (6). Accordingly, one can take any partial contribution, for example the contribution of different subsets of diagrams, then calculate only the terms satisfying this linear identity, and ignore the violating terms. As a consequence, as we showed, this technique helps getting more compact answers for the physical amplitudes. We stress the generality of the proposed technique. For comparison, we refer to the paper [19], where the same (QED gauge invariant) contributions to the crossed process  $e^+e^- \rightarrow \gamma H$  were obtained by choosing an *ad hoc* special set of standard matrix elements.

There is another advantage of the adopted decomposition. Our main goal here is to demonstrate the usefulness of the process  $e\gamma \rightarrow eH$  for measuring the  $Z\gamma H$  coupling. Of course, one does not expect that the contribution of the  $Z$ -boson vertices can be separated from the related photon vertices in a  $SU(2)$  gauge invariant way in the standard model. This connects with the presence of the third component of the  $SU(2)$  gauge field in both the  $Z$ -boson and photon

fields. Moreover, one can show that even the box contribution can not be isolated in a  $SU(2)$  gauge invariant way, by comparing the results in the linear 't-Hooft-Feynman gauge used here, with the nonlinear gauge results (see details in [17]). However, we will see in the next section that the contribution of the box diagrams to the cross section is in general rather small. Hence, the most important issue is the separation of the  $Z\gamma H$  and  $\gamma\gamma H$  vertices. In general, if one wants to compare the relative contributions of the  $Z\gamma H$  and  $\gamma\gamma H$  vertices, one needs to specify the gauge in which one works.

Note, that it is possible that there are new non-standard particles circulating in the loops of the  $Z\gamma H$  and  $\gamma\gamma H$  Green functions, giving additional contributions to the ones of the standard-model electroweak theory. Hence, measuring the corresponding amplitudes could give us some hints on the nature of the actual extension of the standard model.

In case the new scenario implies the non-decoupling regime for the Higgs boson interaction with the new particles, we can use an effective point-like interaction Lagrangian to calculate the contributions of the new physics. In [21, 22], the relevant lagrangian terms were classified and parameterized using five anomalous coupling constants. Of course, these terms must be  $SU(2) \times U(1)$  gauge invariant, and, hence, transversal with respect to the photon momentum. The same is true for their contributions to the  $Z\gamma H$  and  $\gamma\gamma H$  Green functions and to the cross section of the process under discussion. As a consequence, from a kinematical point of view, this type of new physics would contribute similarly to the QED gauge-invariant contributions of the standard  $Z\gamma H$  and  $\gamma\gamma H$  Green functions. Thus, our strategy in the next sections will be to find out the kinematical regions where the relative contribution of the transversal  $Z\gamma H$  Green function is enhanced in comparison with the  $\gamma\gamma H$  one.

Alternative cases, where the Higgs boson interacts with the new particles in the decoupling limit, can not be described by an effective point-like Lagrangian, and some different strategy is necessary to extract the contributions of the corresponding  $Z\gamma H$  and  $\gamma\gamma H$  induced vertices (see [11], for the case of the minimal supersymmetrical extension of the standard model). In these cases, there could be some kind of common agreement to define the different contributions. For instance, our decomposition in eq.(13) could make the job. Consequently, the analysis of the numerical results and kinematical cuts made in the following should be of some help for the measurement of the  $Z\gamma H$  induced vertex in decoupling cases, too.

### 3 Exact cross sections

In this section, we present the total rates  $\sigma(He)$  for the process  $e\gamma \rightarrow eH$  versus the Higgs boson mass  $m_H$  and the c.m.  $e\gamma$  collision energy  $\sqrt{s}$ . We also compare them with the cross sections for the competing tree-level process  $e\gamma \rightarrow H\nu_e W$ [23]. A possible strategy for enhancing the  $Z\gamma H$  vertex effects with respect to the dominant  $\gamma\gamma H$  contribution is then outlined.

In order to correctly relate our exact results to the previous approximate estimates, one

should take into account that in our paper we always assume an exactly monochromatic initial photon beam. It has been customary for some time to present total rates convoluted with a particular form of the initial-photon energy spectrum [4]. On the other hand, presenting unfolded results can help in distinguishing the physical effects related to the particular collision process from details depending on the final realization of the backscattered laser beam, that could evolve with time before the final project of the linear collider is approved <sup>§</sup>.

In our numerical results, we assume  $\alpha(m_e) = 1/137$  in each vertex that involves an on-shell (or almost on-shell) photon. On the other hand, we express both purely electroweak vertices and vertices involving off-shell photons (exchanged in the  $t$  channel when  $p_T^H \gtrsim 10\text{GeV}$ ) in terms of  $\alpha(M_W) = 1/128$ . This is made in a gauge invariant way, i.e. by just rescaling the final cross sections. Also, we assumed  $M_Z = 91.187\text{GeV}$ ,  $\sin^2 \theta_W = 0.2247$ , and, for the top-quark and  $b$ -quark masses,  $m_t = 175\text{GeV}$  and  $m_b = 4.3\text{GeV}$ , respectively.

In figure 6, the total (unpolarized) cross sections for the one-loop process  $e\gamma \rightarrow eH$  (obtained by integrating the analytical formulae in section 2) and the tree-level Higgs production  $e\gamma \rightarrow H\nu_e W$  (computed by CompHEP [25]) are plotted versus  $m_H$ , for  $\sqrt{s} = 500$  and  $800$  GeV. Numerical results can also be found in table 1, where the  $m_H$  dependence of the two channels is reported for  $\sqrt{s} = 0.5, 1$  and  $1.5$  TeV.

One can see that the process  $e\gamma \rightarrow eH$  is characterized by relatively large rates. For instance, for  $m_H$  up to about  $400$  GeV, one finds  $\sigma(He) > 1$  fb, which, for an integrated luminosity of about  $100\text{fb}^{-1}$ , corresponds to more than 100 events. Note also that the cross section for the crossed process  $e^+e^- \rightarrow H\gamma$  has a similar behaviour with  $m_H$ , but is only about a fraction ( $\frac{1}{200} \div \frac{1}{400}$ ) of  $\sigma(He)$ , in the range  $m_H = (100 \div 400)\text{GeV}$  at  $\sqrt{s} = 500\text{GeV}$  [19]. Moreover, contrary to  $\sigma(He)$ ,  $\sigma(H\gamma)$  drops as  $1/s$  at large c.m. collision energies.

At  $\sqrt{s} \simeq 500$  GeV, the  $e\gamma \rightarrow eH$  rate increases with  $m_H$  up to  $m_H \simeq 2M_W$ , where  $\sigma(He) \simeq 21\text{fb}$ . For larger masses, the cross section falls, but more slowly than in the  $\sigma(H\nu W)$  case. As a result,  $\sigma(He) > \sigma(H\nu W)$  for  $m_H \gtrsim 180$  GeV.

At larger  $\sqrt{s}$ ,  $\sigma(He)$  increases, but only slightly. On the other hand,  $\sigma(H\nu W)$  takes much advantage by a larger c.m. collision energy and, e.g., at  $\sqrt{s} = 1\text{TeV}$  and  $m_H = 180\text{GeV}$ , is more than a factor 4 larger than the corresponding  $e\gamma \rightarrow eH$  cross section (cf. table 1).

We also compared the exact rates for  $e\gamma \rightarrow eH$  with the rates one obtains in the Weizsäcker-Williams (WW) approximation according to the approach of [15]. We have found that the WW approximation differs from the exact rate by less than 15% in the range  $\sqrt{s} = 0.5 - 1.5\text{TeV}$ , working better at lower  $\sqrt{s}$  and higher  $m_H$ . For instance, at  $\sqrt{s} = 500\text{GeV}$  and  $m_H = 300\text{GeV}$ , the WW cross section is larger than the exact one by only 3.4%. Anyhow, by adopting an improved WW approach [26], one reaches an accuracy better than the 6% in the same  $\sqrt{s}$  range.

Note also that the difference in the relative importance of the two channels  $e\gamma \rightarrow eH$  and

---

<sup>§</sup>That was recently stressed by V.I. Telnov [24].

$e\gamma \rightarrow H\nu_e W$  in figure 6 with respect to figure 1 of [15] is mainly due to the inclusion of a spectrum for the photon beam [4] in the latter case. Indeed, the photon spectrum considered depletes considerably  $\sigma(H\nu W)$ , while  $\sigma(He)$  keeps relatively stable.

In figure 7, we show separately the contributions to the total cross section for  $e\gamma \rightarrow eH$  given by the squared amplitudes corresponding to the subsets of Feynman diagrams “ $\gamma\gamma H$ ”, “ $Z\gamma H$ ” and “BOX” (defined in section 2). Even if this separation is by no means formally rigorous (and neglects the relative interference effects), it can help in getting a feeling of the relative importance of triangular vertices and box contributions to the total cross section. In figure 7, the upper solid (dashed) curve corresponds to the total cross section at  $\sqrt{s} = 0.5(1.5)\text{TeV}$ . The slightly lower curve shows the largely dominant contribution from the  $\gamma\gamma H$  vertex graphs, while the  $Z\gamma H$  and BOX cross sections are a factor about 50(45) and 150(500) smaller, respectively, for  $m_H \sim 150\text{GeV}$  and  $\sqrt{s} = 0.5(1.5)\text{TeV}$ . At larger  $m_H$ , this pattern keeps qualitatively similar.

In principle, the  $e\gamma \rightarrow eH$  total cross section (and its main contribution from  $\gamma\gamma H$ ) is of the same order of magnitude of the total rates for Higgs production in  $\gamma\gamma$  collisions [13]. Indeed, the expected resolution on the beam energy smears the higher peak cross section over a width much larger than the Higgs resonance. As a result, the channel  $e\gamma \rightarrow eH$  has a comparable potential with respect to the process  $\gamma\gamma \rightarrow H$  in testing the  $\gamma\gamma H$  vertex, as far as the production rates are concerned. In this paper, on the other hand, we would like to concentrate on the problem of disentangling the  $Z\gamma H$  vertex effects, which are out of the  $\gamma\gamma$ -collision domain.

In figure 8, we show a possible strategy to enhance the  $Z\gamma H$  vertex effects in the  $He$  production rate. This consists in requiring a final electron (positron) tagged at large angle. The corresponding cut on the transferred squared momentum  $t$  depletes mainly the amplitudes involving a photon propagator in the  $t$  channel. This can be easily seen from the three plots in figure 8, where the cross sections dependence on  $\sqrt{s}$ , for  $m_H = 120\text{GeV}$ , is shown for no cut on the electron transverse momentum  $p_T^e$  (a), for a cut  $p_T^e > 10\text{GeV}$  (b), and a cut  $p_T^e > 100\text{GeV}$  (c). The relative weight of the  $Z\gamma H$  and BOX contributions with respect to the total cross section is considerably enhanced by a cut on the minimum allowed  $p_T^e$ . For  $p_T^e > 100\text{GeV}$ ,  $Z\gamma H$  is about 60% of  $\gamma\gamma H$ , and  $Z\gamma H$  gives a considerable fraction of the total production rate, which still is sufficient to guarantee investigation (about 0.7 fb). One can also notice that the BOX contribution is of some relevance only in the lower  $\sqrt{s}$  range.

Note that the slight increase in the  $Z\gamma H$  and BOX “cross sections” when going from figure 8 (a) to figure 8 (b) is due to the change of a factor  $\alpha(m_e)^2$  into  $\alpha(M_W)^2$ , which, as previously mentioned, we adopt for large- $p_T^e$  configurations.

We stress that, in the inclusive  $He$  production, the bulk of the events are characterized by a forward final electron escaping detection. On the other hand, requiring a large  $p_T^e$  corresponds, from an experimental point of view, to selecting a different final-state configuration, where the Higgs decay products have a large total transverse momentum, balanced by a high-energy electron detected at large angle.

## 4 Background processes

Assuming a final electron tagged at large transverse momentum in  $e\gamma \rightarrow eH$ , we now address the issue of separating the signal coming from an intermediate mass Higgs (i.e., with  $90\text{GeV} \lesssim m_H \lesssim 140\text{GeV}$ ) from the most important background channels. We recall that the main decay mode for an intermediate mass Higgs is through the channel  $H \rightarrow b\bar{b}$ , with a branching fraction of about 85%.

An in-depth discussion of the problem has been presented in [15] in the different case of a collinear (undetected) final electron, where one can adopt the WW approximation approach. As we have already stressed, the latter is not useful for distinguishing  $Z\gamma H$  vertex effects.

The main irreducible background to the process  $e\gamma \rightarrow eH \rightarrow e(b\bar{b})$  comes from the channel  $e\gamma \rightarrow ebb$ . In the latter, a  $b$  quark pair is produced either through the decay of a virtual  $\gamma(Z)$  or via the fusion of the initial  $\gamma$  with a (virtual)  $\gamma$  or  $Z$  radiated by the electron beam. The complete set of Feynman diagrams is given by 8 graphs and is shown in figure 5.

A crucial parameter to set the importance of the  $e\gamma \rightarrow ebb$  background is the experimental resolution on the  $b\bar{b}$  invariant mass  $\Delta m_{b\bar{b}}$ . The background rates we present here are obtained by integrating the  $m_{b\bar{b}}$  distribution over the range  $m_H - \Delta m_{b\bar{b}} < m_{b\bar{b}} < m_H + \Delta m_{b\bar{b}}$ . We assume a very good mass resolution on the  $b$  quark pair, i.e.  $\Delta m_{b\bar{b}} = 3\text{GeV}$ . Reaching a good resolution on  $m_{b\bar{b}}$  can be actually easier in the  $eH$  production at large angle. Indeed, the tagging of the final electron  $e_f$  implies the possibility of determining its energy with good accuracy. This reflects into an indirect (additional) determination of  $m_{b\bar{b}}$  through the relation

$$E(e_f) = \frac{s - m_{b\bar{b}}^2}{2\sqrt{s}}.$$

Assuming a monochromatic photon beam and neglecting ISR effects (i.e. assuming a fixed  $s$ ), the latter implies a direct connection between the  $m_{b\bar{b}}$  resolution and the  $e_f$  energy resolution, which can help in improving  $\Delta m_{b\bar{b}}$  in the final state configuration considered here (see also [27]).

We now carry out a detailed analysis of the background from  $e\gamma \rightarrow ebb$ . We use CompHEP to generate the kinematical distributions and cross sections. As anticipated, all the rates presented are obtained by integrating the  $m_{b\bar{b}}$  distribution over the range  $m_H - \Delta m_{b\bar{b}} < m_{b\bar{b}} < m_H + \Delta m_{b\bar{b}}$ , with  $\Delta m_{b\bar{b}} = 3\text{GeV}$ . As for the signal rates, we obtain the distributions for the process  $e\gamma \rightarrow eH \rightarrow e(b\bar{b})$  by convoluting the  $H$  distribution for  $e\gamma \rightarrow eH$  with an isotropic (in the Higgs rest frame) decay  $H \rightarrow b\bar{b}$ , with proper branching ratio. This chain, too, is implemented in a modified version of CompHEP, that generates events according to the exact one-loop matrix element for  $e\gamma \rightarrow eH$ .

In figure 9, the upper solid and dot-dashed histograms show the  $p_T^e$  distributions for the signal and background, respectively, for  $m_H = 120\text{GeV}$  and  $\sqrt{s} = 500\text{GeV}$ . The background is considerably larger than the signal, especially at moderate values of  $p_T^e$ . A possible way to

improve this picture is by putting a cut on the angles between each  $b$  and the initial beams. In fact, the vector couplings that characterize the  $b$ 's in the channel  $e\gamma \rightarrow e b \bar{b}$  give rise to a  $b$  angular distribution considerably more forward-backward peaked than in the case of the scalar  $H b \bar{b}$  coupling relevant for the signal. In figure 9, the arrows show the lowering of the  $p_T^e$  distributions, when an angular cut  $\theta_{b-beam} > 18^\circ$  is applied between each  $b$  quark and both the beams. This particular value of the angular cut reduces the signal and background distributions at a comparable level, without penalizing appreciably the signal rate at large  $p_T^e$ . Note that the cut  $\theta_{b-beam} > 18^\circ$  has been optimized at  $\sqrt{s} = 500\text{GeV}$ . Lower angular cuts will be more convenient at larger  $\sqrt{s}$ .

Since, we are interested in isolating  $Z\gamma H$  effects, in figure 10 we compare the same  $p_T^e$  distribution of the signal (and the corresponding effect of the  $\theta_{b-beam}$  cut) with the distribution coming from the pure squared  $Z\gamma H$  amplitude. One can check that the latter is concentrated at large  $p_T^e$  values, which is a typical effect of the massive  $Z$  propagator in the  $t$  channel. The corresponding contribution to the total rate is practically unaltered if one imposes a cut  $p_T^e \gtrsim 50\text{GeV}$ ,

A further source of background for the process  $e\gamma \rightarrow eH \rightarrow e(b\bar{b})$  is the charm production through  $e\gamma \rightarrow ec\bar{c}$ , when the  $c$  quarks are misidentified into  $b$ 's. This reducible background can be cured by a good  $b$ -tagging efficiency, that should control a charm production rate that can be even more than a factor 10 larger than the corresponding  $e\gamma \rightarrow eb\bar{b}$  cross section, depending on the particular kinematical configuration [15]. We computed the rate for  $e\gamma \rightarrow ec\bar{c}$ . By assuming a 10% probability of misidentifying a  $c$  quark into a  $b$  (hence, considering only a fraction 1/10 of the computed  $e\gamma \rightarrow ec\bar{c}$  rate), we find that this reducible background has lower rates than the irreducible one. This can be seen in table 2, where the signal is compared with both the reducible and irreducible background, for two different sets of kinematical cuts, that enhance the  $Z\gamma H$  contribution, and  $m_H = 120\text{ GeV}$ , at  $\sqrt{s} = 500\text{ GeV}$ . Different initial polarizations for the  $e$  beam are considered (see section 5). For unpolarized beams and  $p_T^e > 100\text{GeV}$ , the  $e\gamma \rightarrow ec\bar{c}$  “effective rate” is less than 1/3 on the  $e\gamma \rightarrow eb\bar{b}$  rate. Note that the  $e\gamma \rightarrow ec\bar{c}$  channel is kinematically similar to  $e\gamma \rightarrow eb\bar{b}$ . Hence, the particular strategies analyzed here to reduce the latter automatically depletes also the former.

A further background, that was considered in [15], is the resolved  $e\gamma(g) \rightarrow eb\bar{b}$  production, where the photon interacts via its gluonic content. Its estimate depends on the particular assumption for the gluon distribution in the photon, that is presently poorly known. We anyway tried to evaluate also this possible background, by assuming that the gluon distribution in the photon beam is given by the parameterization [28] (where we have set the energy scale  $Q^2$  in the structure functions equal to  $4m_b^2$ )<sup>¶</sup>. For instance, for the same set of kinematical cuts, and the same  $m_H$  and  $\sqrt{s}$  values assumed in table 2, we have found that  $e\gamma(g) \rightarrow eb\bar{b}$  contributes to the background with rates of  $9.6 \cdot 10^{-3}\text{ fb}$  and  $0.40\text{ fb}$ , for  $p_T^e > 100$  and  $10\text{ GeV}$ , respectively (and unpolarized beams). We also evaluated the contribution from the  $c$  quark production by resolved photons, by  $e\gamma(g) \rightarrow ec\bar{c}$ . Assuming, as above, a 10% probability of misidentifying a  $c$  into a  $b$ , and the same kinematical cuts, the corresponding rate are  $2.8 \cdot 10^{-3}\text{ fb}$  and  $0.16\text{ fb}$ , for

---

<sup>¶</sup>This choice of the scale among possible others tends to maximize the resolved-photon rate.



$p_T^e > 100$  and  $10$  GeV, respectively (and unpolarized beams). The rates presented here derive from a leading-order parameterization of the photon structure functions in [28]. We checked that a higher-order parameterization rises the results by at most 10%. Compared to the direct photon contributions reported in table 2, the resolved photon background should hence only marginally alter the signal to background ratio, especially at large  $p_T^e$  <sup>||</sup>.

In the following, we will restrict to consider the irreducible  $e\gamma \rightarrow e b \bar{b}$  background, being confident that, at large values of the  $p_T^e$  where the  $Z\gamma H$  effects are enhanced, the latter provides the dominant component to the  $e\gamma \rightarrow eH$  background.

## 5 Beam-polarization effects

One of the advantages of a linear collider is the possibility to work with polarized beams. This may allow, on the one hand, to test the parity structure of the interactions governing a particular process and, on the other hand, to optimize its background suppression. Here, we consider the possibility of having either the electron or the photon beam longitudinally polarized.

In figures 11 (a) and (b), for  $m_H = 120\text{GeV}$  and versus  $\sqrt{s}$ , we show the total cross section (and its  $\gamma\gamma H$ ,  $Z\gamma H$  and BOX components) for the unpolarized case (solid) and a completely longitudinally polarized electron (dashed). In particular figure 11 (a) refers to a left-handed electron beam ( $P_e = -1$ ), while figure 11 (b) presents the case of a right-handed electron ( $P_e = +1$ ). While the  $\gamma\gamma H$  curve is unaltered by a  $P_e \neq 0$  value, the total cross section is slightly modified by the influence of the electron polarization on the parity non-conserving  $Z\gamma H$  and BOX couplings. In particular, a left(right)-handed electron beam increases (decreases)  $\sigma_{tot}$ , the  $Z\gamma H$  and the BOX contribution by about 11%, 20% and 100%, respectively, at  $\sqrt{s} = 500\text{GeV}$ . The strong variation in the BOX component is produced by the dominance of the  $W$ -box sector in this contribution.

In figures 11 (c) and (d), the same plots are given when a cut  $p_T^e > 100\text{GeV}$  is applied on the final electron transverse momentum. One can see that in the high  $p_T^e$  sector of the phase-space, the total rates are much more sensitive to the electron polarization. For instance, assuming  $P_e = -1$  ( $P_e = +1$ ) the total rate increases (decreases) by about 94% at  $\sqrt{s} = 500\text{GeV}$ .

Some insight into this result can be gained by looking at tables 3 and 4, where the  $e/\gamma$  polarization dependence of the interference pattern of the  $\gamma\gamma H$ ,  $Z\gamma H$  and BOX contributions is shown for  $p_T^e > 10\text{GeV}$  and  $p_T^e > 100\text{GeV}$ , respectively, at  $\sqrt{s} = 500\text{GeV}$ . For instance, one can see that for  $P_e = +1$  there is a strong destructive interference between the terms  $\gamma\gamma H$  and  $Z\gamma H$ . This is essentially due to the different sign of the couplings  $ee\gamma$  and  $e_R e_R Z$ , where  $e_R$

---

<sup>||</sup>The resolved photon rates above include only the gluon content of the initial photon beam. The contribution coming from the gluon content of the virtual photon, that can be radiated by the initial electron, is not included here. This is anyway expected to be less important than the former contribution.

stands for the right-handed electron component (see also section 2).

The fact that a longitudinal polarization of the electron beam affects drastically the large  $p_T^e$  range can also be clearly seen in figure 12, where the  $p_T^e$  distributions relative to the unpolarized and to the left-handed and right-handed polarized  $e$  beam are presented for the signal and the  $e\gamma \rightarrow e b \bar{b}$  background. One can also see that, although both the signal  $S$  and background  $B$  are increased by a left-handed polarization, the ratio  $S/B$  is improved at large  $p_T^e$ .

Figures 13 (a), (b), (c) and (d) show the effects of assuming a longitudinally polarized photon beam in the same framework of figures 11. The trend is similar to the polarized  $e$  case, but the effect is quantitatively more modest for a polarized  $\gamma$ , especially at large values of  $\sqrt{s}$ . The only exception is given by the BOX contribution that is still considerably altered by  $P_\gamma \neq 0$  at any  $\sqrt{s}$ .

## 6 Initial State Radiation effects

The effects of the ISR on the signal and the background rates can be taken into account by folding the corresponding cross sections with a structure function describing the reduction of the electron beam energy because of the QED radiation. We adopt the approach of [29], that is accurate at the next-to-leading order for collinear emission and resums soft photon effects. All this is implemented through the computer package CompHEP, which automatically takes into account also the kinematical cuts needed either to enhance the  $Z\gamma H$  contribution in the signal (i.e.,  $p_T^e$  cuts) or to decrease the relative importance of the background (i.e.,  $\theta_{b-beam}$  cuts).

We compared the rates of the unfolded cross sections with the cross sections convoluted with the ISR structure function. The effect of the ISR in our context has been found to be marginal in general. In particular, we found that the ISR effects slightly reduce the signal for all the electron polarization states. For the kinematical configurations described in table 2, the signal is reduced by about 3%, for  $p_T^e > 100\text{GeV}$  and even less (about 1%) for  $p_T^e > 10\text{GeV}$ . On the other hand, the irreducible  $e\gamma \rightarrow e b \bar{b}$  background is a little enhanced by the ISR. For  $p_T^e > 100\text{GeV}$ , it is increased by less than 1%, while, for  $p_T^e > 10\text{GeV}$ , it raises by about 4%. This holds for both  $P_e = 0$  and  $P_e = \pm 1$ .

We checked that such behaviors can be easily explained in terms of the increasing/decreasing of the relevant cross section with  $\sqrt{s}$ , when all the relevant kinematical cuts are taken into account.

Altogether, one can conclude that the “unfolded” general picture is only mildly modified by the ISR effects.

## 7 Optimization of S/B and electron asymmetries

As can be seen in table 2, a  $p_T^e$  cut of 100 GeV, along with a resolution on  $m_{b\bar{b}}$  of  $\pm 3$  GeV and a cut on all the  $b$ 's that are closer than  $18^\circ$  to the beams, optimizes the  $S/B$  ratio, for  $m_H = 120$  GeV and  $\sqrt{s} = 500$  GeV. In particular, it gives rise to a signal rate of 0.40 (0.78) fb versus an irreducible background rate of 0.63 (0.96) fb in the unpolarized ( $P_e = -1$  polarized) case. This means that the signal and the background are comparable in the interesting configurations. With an integrated luminosity of  $100 \text{ pb}^{-1}$ , the corresponding statistical significance of the signal from  $e\gamma \rightarrow eH$  is of the order  $S/\sqrt{S+B} \simeq 4$  for  $P_e = 0$  and 6, if  $P_e = -1$ . This implies the possibility of measuring the corresponding cross section for  $e\gamma \rightarrow eH$  with an accuracy of about 25% (17% for polarized  $P_e = -1$  beam), unless systematic errors dominate.

Of course, the final accuracy on the determination of the coupling of the Higgs boson to the  $Z$  and  $\gamma$  is not simply the accuracy on the cross-section measurement. As we can see from table 4, for  $p_T^e > 100 \text{ GeV}$  and  $\sqrt{s} = 500 \text{ GeV}$  (and unpolarized beams), the  $Z\gamma H$  vertex contributes about half of the measured cross sections, including the interference effects. Assuming that the Higgs boson coupling with the photons is tested and measured with high accuracy in some different process, the statistical sensitivity to the Higgs coupling with the  $Z$  and  $\gamma$  gets of the order  $\frac{1}{2}S/\sqrt{S+B}$  (note that, assuming a reduced integrated luminosity of  $r100 \text{ pb}^{-1}$ , with  $r < 1$ , would in general lower the expected accuracy by a factor  $\sqrt{r}$ ).

There is a further way to improve the accuracy on the cross section measurement. This is by exploiting the electron angular asymmetry of the signal with respect to the beam. Indeed, we found that in the  $e\gamma \rightarrow e b\bar{b}$  background the final electron angular distribution, although not completely symmetric, is almost equally shared in the forward and backward direction with respect to the beam. In particular, we checked that the 2nd diagram in figure 5 is responsible for the backward peak, while the 4th diagram gives the forward one.

On the contrary, the final electron in  $e\gamma \rightarrow eH$  is mostly directed in the forward direction. The typical behavior is shown in figure 14, where the solid (dashed) line gives the histogram for the final electron angular distribution [in the centre-of-mass system] for the signal (background), for  $p_T^e > 100 \text{ GeV}$  and  $\theta(b - \text{beam}) > 18^\circ$ , at  $m_H = 120 \text{ GeV}$  and  $\sqrt{s} = 500 \text{ GeV}$ . As usual, the background is integrated over the range  $m_H - \Delta m_{b\bar{b}} < m_{b\bar{b}} < m_H + \Delta m_{b\bar{b}}$  with  $\Delta m_{b\bar{b}} = 3 \text{ GeV}$ . The initial beams are assumed to be unpolarized. The strong asymmetry in the signal  $\theta_e$  distribution is manifest. The final electron is mostly scattered forwards in  $e\gamma \rightarrow eH$  (the empty intervals for  $\theta_e \lesssim 25^\circ$  and  $\theta_e \gtrsim 155^\circ$  are just due to the  $p_T^e > 100 \text{ GeV}$  cut). Note that this pattern keeps valid also when relaxing the  $p_T^e$  cut, and for polarized beams.

It is straightforward at this point to enhance the  $S/B$  ratio, by simply measuring the difference between the forward and backward cross sections. In table 5, after applying the same cuts as in table 2 and for different polarizations of the  $e$  beam, we report apart from the total rate, the forward cross sections and the difference of the forward and backward cross sections  $\mathcal{S}_{FB} = \sigma(\theta_e < 90^\circ) - \sigma(\theta_e > 90^\circ)$ . One can see that, in the difference  $\mathcal{S}_{FB}$ , 80% of the signal survives, while the background is reduced by about an order of magnitude, in both

the interesting  $P_e = 0$  and  $P_e = -1$  cases. With a luminosity of  $100 \text{ pb}^{-1}$ , one then gets an accuracy on  $\mathcal{S}_{FB}$  of about 16% for unpolarized  $e$  beams, and 12% for  $P_e = -1$  (corresponding to  $S/\sqrt{S+B} \simeq 6.4$  and  $8.5$ , respectively.) By the way, it could also be convenient to measure the relative asymmetry  $\mathcal{S}_{FB}/[\sigma(\theta_e < 90^\circ) + \sigma(\theta_e > 90^\circ)]$ , that has the advantage of being free from possible uncertainties on the absolute normalization of the cross sections.

The analysis above can be also extended to the study of possible anomalous contributions in the  $Z\gamma H$  amplitude coming from some extension of the standard model. For instance, all models causing a variation in the cross section and/or angular asymmetries by more than about 20% should be easily disentangled in the same experimental conditions analyzed here. Furthermore, since in the latter case what we call here signal could act as a further background, it could be convenient to consider also the  $P_e = +1$  cross sections [35]. Indeed, as shown in table 4, for large  $p_T^e$  the right-handed polarized  $e$  beam minimizes the standard model  $e\gamma \rightarrow eH$  background, because of the strong negative interferences between the different amplitudes.

## 8 Conclusions

The study of the exact rates for the process  $e\gamma \rightarrow eH \rightarrow e(b\bar{b})$  in the intermediate  $m_H$  range confirms that the associated  $He$  production in  $e\gamma$  collisions is a competitive means with respect to the process  $\gamma\gamma \rightarrow H$  to study the vertex  $\gamma\gamma H$  and its possible anomalies (as anticipated by the analysis made in the WW approximation [15]). The relevant total (unpolarized) cross sections are in the range  $(9 \div 17)\text{fb}$ , for  $m_H = (90 \div 150)\text{GeV}$  and  $\sqrt{s} = (0.5 \div 1.5)\text{GeV}$ , which, assuming an integrated luminosity of  $100 \text{ fb}^{-1}$ , corresponds to  $\mathcal{O}(10^3)$  Higgs events.

If the final electron is tagged at large  $p_T^e$ , a further possibility offered by the channel  $e\gamma \rightarrow eH$  is to study the effects coming from the  $Z\gamma H$  vertex, keeping still a reasonable statistics [ $\mathcal{O}(10^2)$  events]. This possibility has not any counterpart in the  $e^+e^-$  and  $\gamma\gamma$  collision physics. Graphs with boxes, too, contribute at large  $p_T^e$ , but their relative importance decreases with  $\sqrt{s}$  for  $\sqrt{s} > 400\text{GeV}$ .

We checked that the main background comes from the process  $e\gamma \rightarrow e b\bar{b}$ . This can be controlled by a good  $m_{b\bar{b}}$  experimental resolution (that can be improved by the final electron energy determination), and by requiring that the final  $b$  quarks be not too close to the beams direction.

We have also shown that starting with a left-handed polarized electron beam doubles the rates and improves the  $S/B$  ratio, in the  $p_T^e \gtrsim 100\text{GeV}$  kinematical range interesting for the  $Z\gamma H$  vertex studies. Further improvements in the  $S/B$  ratio can be obtained by exploiting the final-electron angular asymmetry of the signal.

The inclusion of the initial state radiation effects marginally deteriorates the  $S/B$  ratio.

The value of the integrated luminosity assumed in this study (that is  $100 \text{ fb}^{-1}$ ) does not

seem to be essential to disentangle a  $Z\gamma H$  effect, although a high luminosity would be crucial to increase the accuracy of the measurement. With a luminosity of  $100\text{ fb}^{-1}$ , one expects an accuracy as good as about 10% on the measurement of the  $Z\gamma H$  effects, at  $\sqrt{s} = 500\text{ GeV}$ . A luminosity of  $50\text{ fb}^{-1}$  would anyhow allow to measure the standard model signal with an accuracy better than 20%.

In conclusion, the  $e\gamma \rightarrow eH \rightarrow e(b\bar{b})$  turns out to be an excellent means to check the standard-model one-loop coupling  $Z\gamma H$ . Further investigation and comparison with the predictions from possible extensions of the standard model altering the  $Z\gamma H$  vertex is worthwhile. This, we are planning to do in a forthcoming paper [35].

## Acknowledgements

Useful discussions with I.F. Ginzburg and A.E. Pukhov are gratefully acknowledged. We also wish to thank I.P. Ivanov and A.T. Banin for their independent check of our results. The work of V.A.I. was partly supported by the Grants INTAS-93-1180ext and 96-02-18635 from the Russian Fund for Basic Research. V.A.I. wishes also to thank INFN for its hospitality and the possibility to work during his visit at the University of Roma 1.

# Appendix

In this appendix, we give the explicit expressions for the functions  $B_0$ ,  $C_0$  and  $D_i$  appearing in eqs. (15), (20) and (21). Next, we give a short discussion on some sources of numerical instabilities arising in the computation of the total cross section, and describe the method used to control them.

## • Loop integrals

The complete set of independent loop integrals used in our calculations is defined by the following formulas in dimensional regularization<sup>\*\*</sup>, where the time-space dimension is  $n = 4 - 2\varepsilon$ :

$$B_0(p^2, m^2, m^2) \equiv \frac{1}{i\pi^2} \int \frac{d^n q}{[m^2 - q^2][m^2 - (q + p)^2]}, \quad (25)$$

$$C_0(m, p_1, m, p_2, m) \equiv \frac{1}{i\pi^2} \int \frac{d^n q}{[m^2 - q^2][m^2 - (q + p_1)^2][m^2 - (q + p_2)^2]}, \quad (26)$$

$$D_{0;\mu;\mu\nu}(m_0, p_1, m_1, \dots, p_3, m_3) \equiv \frac{1}{i\pi^2} \int \frac{\{1; q_\mu; q_\mu q_\nu\} d^n q}{[m_0^2 - q^2][m_1^2 - (q + p_1)^2] \dots [m_3^2 - (q + p_3)^2]}. \quad (27)$$

Of course, each denominator factor originated from the propagators should be treated in the Feynman limit:  $(M^2 - p^2)^{-1} \equiv \lim_{\epsilon \rightarrow 0} (M^2 - p^2 - i\epsilon)^{-1}$ . As a result, these loop integrals have complex values in general.

We decompose the vector and tensor box-integrals over the covariant Lorentz structures:

$$\begin{aligned} D^\mu &\equiv p_1^\mu \cdot D_1 + p_2^\mu \cdot D_2 + p_3^\mu \cdot D_3, \\ D^{\mu\nu} &\equiv g^{\mu\nu} \cdot D_{00} + p_1^\mu p_1^\nu \cdot D_{11} + p_2^\mu p_2^\nu \cdot D_{22} + p_3^\mu p_3^\nu \cdot D_{33} \\ &\quad + (p_1^\mu p_2^\nu + p_2^\mu p_1^\nu) \cdot D_{12} + (p_1^\mu p_3^\nu + p_3^\mu p_1^\nu) \cdot D_{13} + (p_2^\mu p_3^\nu + p_3^\mu p_2^\nu) \cdot D_{23}. \end{aligned} \quad (28)$$

Note that all these integrals are UV finite. The only exception is  $B_0$ , for which  $\lim_{\varepsilon \rightarrow 0} \varepsilon B_0 = 1$ . In our results, the integrals  $B_0$  appear in the triangle contributions only in a UV finite combination [see eq. (15)].

For the numerical evaluation of the scalar loop integrals, as well as of the scalar factors in the decomposition (28), we used the FF library [32], and the corresponding Fortran routines. Note that in our definition of the loop integrals, the  $C$ -type integrals have an opposite sign with

---

<sup>\*\*</sup>Relations to other definitions of one-loop integrals:

- Our definition of integrals corresponds to the *Passarino-Veltman* integrals [30] if metric signature is changed from  $(-+++)$ , used by Passarino-Veltman, to  $(+---)$ . They also used a different choice of external momenta, hence their decomposition (28) differ from ours.
- We differ from [31] by an opposite sign of the  $C$ -integrals.

respect to the latter. Moreover, in the decomposition (28) we use a set of external momenta different from the FF library. Hence, we perform a linear transformation of our scalar factors  $D_i$  and  $D_{ij}$ , in order to get a connection with the corresponding factors defined in the FF library.

Regarding the analytical evaluation of the amplitudes, the check of the QED gauge-invariance identities (6), as well as the extraction of the QED gauge non-invariant terms (22) and the corresponding ones coming from the  $W$ -box diagrams, we used the computer algebra system REDUCE [33].

### • Numerical instabilities

Although, in general, we computed the relevant amplitudes in the  $m_e = 0$  chiral limit, in the calculation of the total cross section we assumed for  $t_{max}$  the exact value, that is approximately equal to  $(-m_e^2 m_H^4 / s^2)$ . Then, when integrating the region near the  $t$ -channel pole at  $t \simeq 0$  with routines in double precision for arithmetic operations, we met some numerical instabilities. In particular, we observed a lost of numerical precision in the evaluation of the kinematics for  $t \geq -10^{-9} \text{GeV}^2$ . In order to avoid this instability, we used the following procedure. We introduced some parameter  $t_0$  and approximated the matrix element  $M$  for the  $t$ -channel photon contribution by  $M = X(t)/t$  for  $t \leq t_0$ , and  $M = X(t_0)/t$  for  $t_0 \leq t \leq t_{max}$ , where  $X(t)$  is the numerator of the matrix element. If the parameter  $t_0$  is taken close to  $t_{max}$ , the latter turns out to be a good approximation, since then  $X(t_{max})$  differs very little from  $X(t_0)$ . To test this method, we checked the independence of the total cross section from the parameter  $t_0$ , by varying  $t_0$  in the interval  $-1 \text{ GeV}^2 \leq t_0 \leq -10^{-6} \text{GeV}^2$ .

There is also a second source of numerical instability when the  $W$  and  $Z$ -box diagrams are evaluated near  $t = 0$  and  $u = 0$ . When the tensor integrals for the boxes are expressed via the scalar integrals by Passarino-Veltman [30] (e.g., FF library uses this procedure [32]) some spurious poles can arise from different terms. Of course, in the total results these poles cancel each other. In our case such spurious poles arise at  $t = 0$  and  $u = 0$ . We checked analytically the corresponding cancellation in our results for the boxes (18,19). First, we expressed the formulas (19) via scalar integrals and then analyzed the final expressions in  $t = 0$  and  $u = 0$ , where they must vanish. This analysis was made with the help of the REDUCE program PV [34], that implements the Passarino-Veltman procedure. Anyhow, it is not possible to check explicitly the cancellation of these spurious poles at the level of the scalar integrals. As a result, these integrals cannot be evaluated with good accuracy at  $t \geq -10^{-6} \text{GeV}^2$ , since the numerical precision of the FF library is not sufficient to get this cancellation. Fortunately, one can neglect the box contributions at such small  $t$  and  $u$ , since these functions have a regular behaviour near  $t = 0$  and  $u = 0$ . Therefore, we just neglected the  $W$  and  $Z$ -box contributions for  $t, u \geq -10^{-2} \text{GeV}^2$ .

## References

- [1] A. Blondel, *Status of the Electroweak Interactions*, Plenary talk at the 28th International Conference on High Energy Physics, Warsaw, Poland, 25-31 July 1996.
- [2] Proceedings, *Physics and Experiments with  $e^+e^-$  Linear Colliders*, Saariselkä 1991, eds R. Orava P. Eerola and M. Nordberg (World Scientific 1992);  
Proceedings, *Physics and Experiments with  $e^+e^-$  Linear Colliders*, Waikoloa/Hawaii 1993, eds. F. Harris, S. Olsen, S. Pakvasa and X. Tata (World Scientific 1993);  
Proceedings, *Physics and Experiments with  $e^+e^-$  Linear Colliders*, Morioka 1995, eds. A. Miyamoto, Y. Fujii, T. Matsui and S. Iwata (World Scientific 1996).
- [3] Proceedings,  *$e^+e^-$  Collisions at 500 GeV: The Physics Potential* 1991/93, DESY Reports 92-123 A+B, and 93-123 C, P.M. Zerwas ed.; Proceedings,  *$e^+e^-$  Collisions at TeV Energies: The Physics Potential* 1995, DESY Report 96-123 D, P.M. Zerwas ed.
- [4] I.F. Ginzburg, G.L. Kotkin, V.G. Serbo and V.I. Telnov, Nucl.Instr. Methods 205 (1983) 47;  
I.F. Ginzburg, G.L. Kotkin, S.L. Panfil, V.G. Serbo and V.I. Telnov, Nucl.Instr. Methods 219 (1984) 5;  
V.I. Telnov, Nucl.Instr. Methods A 294 (1990) 72.
- [5] Proceedings, Workshop on *Gamma-Gamma Colliders*, Berkeley 1994, Nucl. Instr. Meth. A355 (1995) 19.
- [6] J.F. Gunion, H.E. Haber, G. L. Kane and S. Dawson, *The Higgs Hunter's Guide* (Addison-Wesley, New York, 1990).
- [7] H.M. Georgi, S.L. Glashow, M.E. Machacek and D.V. Nanopoulos, Phys. Rev. Lett. 40 (1978) 692;  
A. Djouadi, M. Spira and P.M. Zerwas, Phys. Lett. B264 (1991) 440;  
S. Dawson, Nucl. Phys. B359 (1991) 283;  
M. Spira, A. Djouadi, D. Graudenz and P.M. Zerwas, Nucl. Phys. B453 (1995) 17.
- [8] J. Ellis, M.K. Gaillard and D.V. Nanopoulos, Nucl. Phys. B106 (1976) 292;  
M.A. Shifman, A.I. Vainshtein, M.B. Voloshin, V.I. Zakharov, Sov. J. Nucl. Phys. 30 (1979) 711.
- [9] L. Bergstrom and G. Hulth, Nucl. Phys. B259 (1985) 137; ERRATUM *ibid* B276 (1986) 744.
- [10] F. Wilczek, Phys. Rev. Lett. 39 (1977) 1304.
- [11] A. Djouadi, V. Driesen, W. Hollik and A. Kraft, preprint KA-TP-30-1996, PM/96-39, hep-ph/9701342.



- [12] J.F. Gunion and H.E. Haber, Phys. Rev. D48 (1993) 5109;  
O.J.P. Èboli, M.C. Gonzales-Garcia, F. Halzen and D. Zeppenfeld, Phys. Rev. D48 (1993) 1430;  
D.L. Borden, D.A. Bauer and D.O. Caldwell, Phys. Rev. D48 (1993) 4018;  
D.L. Borden,, V.A. Khoze, W.J. Stirling and J. Ohnemus, Phys. Rev. D50 (1994) 4499;  
M. Baillargeon, G. Belanger and F. Boudjema, Phys. Rev. D51 (1995)4712.
- [13] I. Watanabe, Proceedings, *Physics  $e^+e^-$ ,  $e\gamma$  and  $\gamma\gamma$  collisions at linear accelerators*, Tokyo 1994, 139-148, hep-ph/9504226.
- [14] C.F.von Weizsäcker, Z. Phys. 88(1934)612;  
E.J. Williams, Phys. Rev. 45 (1934) 729.
- [15] O.J.P. Èboli and M.C. Gonzales-Garcia, Phys. Rev. D49 (1994) 91.
- [16] D.A. Dicus and W.W. Repko, Phys. Rev. D53 (1996) 3616.
- [17] A. Barroso, J. Pulido and J.C. Romao, Nucl. Phys. B267 (1985) 509; B272 (1986) 693.
- [18] A. Abbasabadi, D. Bowser-Chao, D.A. Dicus and W.A. Repko, Phys. Rev. D52 (1995) 3919.
- [19] A. Djouadi, V. Driesen, W. Hollik and J. Rosiek, Nucl. Phys. B491 (1997) 68.
- [20] A. Denner, J. Kublbeck, R. Mertig, M. Bohm, Z. Phys. C56 (1992) 261.
- [21] W. Buchmüller and D. Wyler, Nucl. Phys. B268 (1986) 621.
- [22] K. Hagiwara et al., Phys. Rev. D48 (1993) 2182.
- [23] E.E. Boos, M.N. Dubinin, V.A. Ilyin, G.V. Jikia, A.E. Pukhov and S.F. Sultanov, Phys. Lett. B273 (1991) 173;  
K. Hagiwara, I. Watanabe and P.M. Zerwas, Phys. Lett. B278 (1992) 187;  
K. Cheung, Phys. Rev. D48 (1993) 1035;  
E. Boos, A. Pukhov, M. Sachwitz and H.J. Schreiber, preprint DESY 96-101 (1996), hep-ph/9610424.
- [24] V.I. Telnov, communication to the Final Meeting of the Joint ECFA/DESY LC Study on *Physics and Detectors for a Linear Collider*, DESY, Nov 20-22,1996, Hamburg.
- [25] P.A. Baikov at al., Proceedings, X Workshop on *High Energy Physics and Quantum Field Theory* (QFTHEP-96), Moscow 1996, ed. B. Levtchenko and V. Sarin, hep-ph/9701412;  
E.E. Boos, M.N. Dubinin, V.A. Ilyin, A.E. Pukhov and V.I. Savrin, preprint SNUTP-94-116, Oct 1994 and Korean Physical Society meeting, Oct 21, 1994, hep-ph/9503280.
- [26] V.M. Budnev et al., Phys. Rep. 15C (1975) 181;  
S. Frixione, M. Mangano, P. Nason and G. Ridolfi, Phys. Lett. B319 (1993) 339.

- [27] P. Mättig, “Status Report of a Study on Higgs + Photon Production in 500 GeV  $e^+e^-$  Collisions”, memorandum, 25 August 1995, unpublished.
- [28] M. Glück, E. Reya and A. Vogt, Phys. Rev. D46 (1992) 1973.
- [29] E.A. Kuraev, V.S. Fadin, Sov. J. Nucl. Phys. 41 (1985) 466;  
S. Jadach, B.F.L. Ward, Comp. Phys. Commun. 56 (1990) 351.
- [30] G. Passarino and M. Veltman Nucl. Phys. B160 (1979) 151.
- [31] A. Denner, Fortschr. Phys. **41** (1993) 307.
- [32] G.J. van Oldenborgh, *FF - a package to evaluate one-loop Feynman diagrams*, NIKHEF-H/90-15, September 1990;  
G.J. van Oldenborgh and J.A.M. Vermaseren, Z. Phys. C46 (1990) 425.
- [33] A. Hearn, J. Fitch, *REDUCE User’s Manual*, v.3.6, RAND Publication CP78(Rev. 7/95).
- [34] V.A. Ilyin and A.P. Kryukov, Preprint INP MSU 97-5/456, 1997.
- [35] E. Gabrielli, V.A. Ilyin and B. Mele, in preparation.

$m_H$ (GeV)	$\sqrt{s}=0.5$ TeV		$\sqrt{s}=1$ TeV		$\sqrt{s}=1.5$ TeV	
	$e\gamma \rightarrow eH$	$e\gamma \rightarrow \nu WH$	$e\gamma \rightarrow eH$	$e\gamma \rightarrow \nu WH$	$e\gamma \rightarrow eH$	$e\gamma \rightarrow \nu WH$
80	8.38	47.3	9.29	157.	9.74	243.
100	8.85	41.3	9.94	148.	10.5	233.
120	9.80	35.4	11.2	138.	11.8	223.
140	11.8	29.8	13.7	129.	14.6	212.
160	21.1	24.6	25.0	120.	26.6	201.
180	20.9	19.9	25.3	111.	27.0	191.
200	17.2	15.7	21.2	102.	22.8	181.
300	5.97	2.87	8.53	65.4	9.43	136.
400	1.64	0.0151	2.78	38.8	3.18	100.
500			0.501	20.9	0.595	72.9
600			0.0767	9.51	0.0952	51.5
700			0.0608	3.23	0.0901	35.0

Table 1: *Total cross sections in fb.*

$m_H = 120 \text{ GeV}$ $\sqrt{s} = 500 \text{ GeV}$	$p_T^e > 100 \text{ GeV}$			$p_T^e > 10 \text{ GeV}$		
	$\sigma(eH) (fb)$	$\sigma(ebb) (fb)$	$\sigma(ec\bar{c}) (fb)$	$\sigma(eH) (fb)$	$\sigma(ebb) (fb)$	$\sigma(ec\bar{c}) (fb)$
$P_e = 0$	0.404	0.634	0.208	1.01	1.34	0.868
$P_e = -1$	0.780	0.961	0.277	1.60	1.94	1.00
$P_e = +1$	0.0263	0.304	0.136	0.429	0.767	0.726

Table 2: Comparison of the signal with the irreducible background  $e\gamma \rightarrow ebb$  and the reducible background coming from  $e\gamma \rightarrow ec\bar{c}$ , for different  $e$ -beam polarizations. For the  $e\gamma \rightarrow ec\bar{c}$  background a 10% probability of misidentifying a  $c$  quark into a  $b$  is assumed (that is, only 1/10 of the cross section is reported). Two configurations for kinematical cuts are considered. The angular cut  $\theta(b(c) - \text{beam}) > 18^\circ$  is applied everywhere. The signal rates includes the complete treatment of the  $H \rightarrow b\bar{b}$  decay. The  $b\bar{b}$  invariant mass for the background is integrated over the range  $m_H - \Delta m_{b\bar{b}} < m_{b\bar{b}}(m_{c\bar{c}}) < m_H + \Delta m_{b\bar{b}}$  with  $\Delta m_{b\bar{b}} = 3 \text{ GeV}$ .

$\sqrt{s} =$ 500GeV	$m_H$ (GeV)	$\sigma(e\gamma \rightarrow eH, p_T^e > 10 \text{ GeV}) \text{ (fb)}$						
		Total	$ \gamma\gamma H ^2$	$ Z\gamma H ^2$	$ \text{box} ^2$	Int. $_{(\gamma\gamma H-Z\gamma H)}$	Int. $_{(\gamma\gamma H-\text{box})}$	Int. $_{(Z\gamma H-\text{box})}$
$(P_e = 0;$ $P_\gamma = 0)$	80	1.85	1.49	0.203	0.0232	0.0765	0.0312	0.0205
	100	1.99	1.61	0.216	0.0237	0.0820	0.0322	0.0212
	120	2.22	1.81	0.238	0.0244	0.0912	0.0340	0.0224
	140	2.68	2.20	0.280	0.0261	0.109	0.0377	0.0252
$(P_e = -1;$ $P_\gamma = 0)$	80	2.72	1.49	0.244	0.0458	0.832	0.0544	0.0476
	100	2.91	1.61	0.260	0.0466	0.892	0.0559	0.0494
	120	3.24	1.81	0.286	0.0481	0.991	0.0586	0.0526
	140	3.89	2.20	0.336	0.0513	1.18	0.0647	0.0590
$(P_e = +1;$ $P_\gamma = 0)$	80	0.979	1.49	0.162	6.78E-04	-0.679	8.02E-03	-6.68E-03
	100	1.06	1.61	0.173	7.06E-04	-0.728	8.53E-03	-7.09E-03
	120	1.19	1.81	0.190	7.50E-04	-0.809	9.31E-03	-7.70E-03
	140	1.46	2.20	0.224	8.18E-04	-0.965	0.0106	-8.72E-03
$(P_e = 0;$ $P_\gamma = -1)$	80	1.94	1.49	0.211	0.0344	0.179	8.59E-03	0.0108
	100	2.10	1.61	0.226	0.0353	0.203	9.64E-03	0.0122
	120	2.36	1.81	0.249	0.0369	0.240	0.0114	0.0145
	140	2.87	2.20	0.294	0.0402	0.307	0.0151	0.0190
$(P_e = 0;$ $P_\gamma = +1)$	80	1.76	1.49	0.195	0.0121	-0.0255	0.0538	0.0302
	100	1.88	1.61	0.207	0.0120	-0.0385	0.0547	0.0301
	120	2.08	1.81	0.227	0.0119	-0.0578	0.0565	0.0303
	140	2.48	2.20	0.266	0.0120	-0.0896	0.0603	0.0313

Table 3: *Interference pattern between the  $\gamma\gamma Z$ ,  $Z\gamma H$  and boxes contributions versus the  $e$ -beam and  $\gamma$ -beam polarizations, for  $p_T^e > 10 \text{ GeV}$ .*

$\sqrt{s} = 500\text{GeV}$	$m_H$ (GeV)	$\sigma(e\gamma \rightarrow eH, p_T^e > 100\text{ GeV})$ (fb)						
		Total	$ \gamma\gamma H ^2$	$ Z\gamma H ^2$	$ \text{box} ^2$	Int. $_{(\gamma\gamma H - Z\gamma H)}$	Int. $_{(\gamma\gamma H - \text{box})}$	Int. $_{(Z\gamma H - \text{box})}$
$(P_e = 0; P_\gamma = 0)$	80	0.516	0.265	0.149	0.0208	0.0393	0.0247	0.0177
	100	0.542	0.278	0.158	0.0210	0.0415	0.0254	0.0182
	120	0.584	0.301	0.171	0.0213	0.0449	0.0268	0.0192
	140	0.668	0.347	0.196	0.0221	0.0517	0.0298	0.0214
$(P_e = -1; P_\gamma = 0)$	80	0.996	0.265	0.179	0.0412	0.428	0.0424	0.0414
	100	1.05	0.278	0.189	0.0414	0.451	0.0435	0.0428
	120	1.13	0.301	0.205	0.0420	0.488	0.0457	0.453
	140	1.29	0.347	0.235	0.0435	0.562	0.0505	0.506
$(P_e = +1; P_\gamma = 0)$	80	0.0364	0.265	0.119	5.13E-04	-0.349	6.97E-03	-6.02E-03
	100	0.0381	0.278	0.126	5.29E-04	-0.368	7.37E-03	-6.37E-03
	120	0.0410	0.301	0.136	5.54E-04	-0.399	8.00E-03	-6.89E-03
	140	0.0471	0.347	0.157	5.93E-04	-0.458	9.05E-03	-7.75E-03
$(P_e = 0; P_\gamma = -1)$	80	0.592	0.265	0.157	0.0302	0.124	7.47E-03	8.53E-03
	100	0.630	0.278	0.166	0.0306	0.137	8.47E-03	9.69E-03
	120	0.692	0.301	0.180	0.0313	0.157	0.0102	0.0116
	140	0.808	0.347	0.208	0.0328	0.192	0.0136	0.0153
$(P_e = 0; P_\gamma = +1)$	80	0.441	0.265	0.142	0.0115	-0.0456	0.0419	0.0269
	100	0.454	0.278	0.149	0.0114	-0.0542	0.0424	0.0268
	120	0.477	0.301	0.161	0.0113	-0.0671	0.0435	0.0268
	140	0.527	0.347	0.184	0.0113	-0.0883	0.0460	0.0275

Table 4: Interference pattern between the  $\gamma\gamma Z$ ,  $Z\gamma H$  and boxes contributions versus the  $e$ -beam and  $\gamma$ -beam polarizations, for  $p_T^e > 100\text{ GeV}$ .

$m_H = 120\text{ GeV}$ $\sqrt{s} = 500\text{ GeV}$	$\sigma(e\gamma \rightarrow eH)\text{ fb}$			$\sigma(e\gamma \rightarrow ebb)\text{ fb}$		
	no $\theta_e$ cut	$\theta_e < 90^\circ$	$\mathcal{S}_{FB}$	no $\theta_e$ cut	$\theta_e < 90^\circ$	$\mathcal{S}_{FB}$
$P_e = 0$	0.404	0.362	0.320	0.634	0.281	-0.072
$P_e = -1$	0.780	0.699	0.618	0.961	0.433	-0.095
$P_e = 1$	0.0263	0.0258	0.0253	0.304	0.126	-0.052

Table 5: Forward-backward asymmetry in the electron scattering angle,  $\theta_e$ , for different  $e$ -beam polarizations. The total cross section, the forward cross section and the difference of the forward and backward cross sections [ $\mathcal{S}_{FB} = \sigma(\theta_e < 90^\circ) - \sigma(\theta_e > 90^\circ)$ ] for the signal and the irreducible background, are presented. The kinematical cuts  $\theta_{b\text{-beam}} > 18^\circ$ ,  $P_t^e > 100\text{ GeV}$  and  $m_H - \Delta m_{b\bar{b}} < m_{b\bar{b}} < m_H + \Delta m_{b\bar{b}}$ , with  $\Delta m_{b\bar{b}} = 3\text{ GeV}$ , are applied.

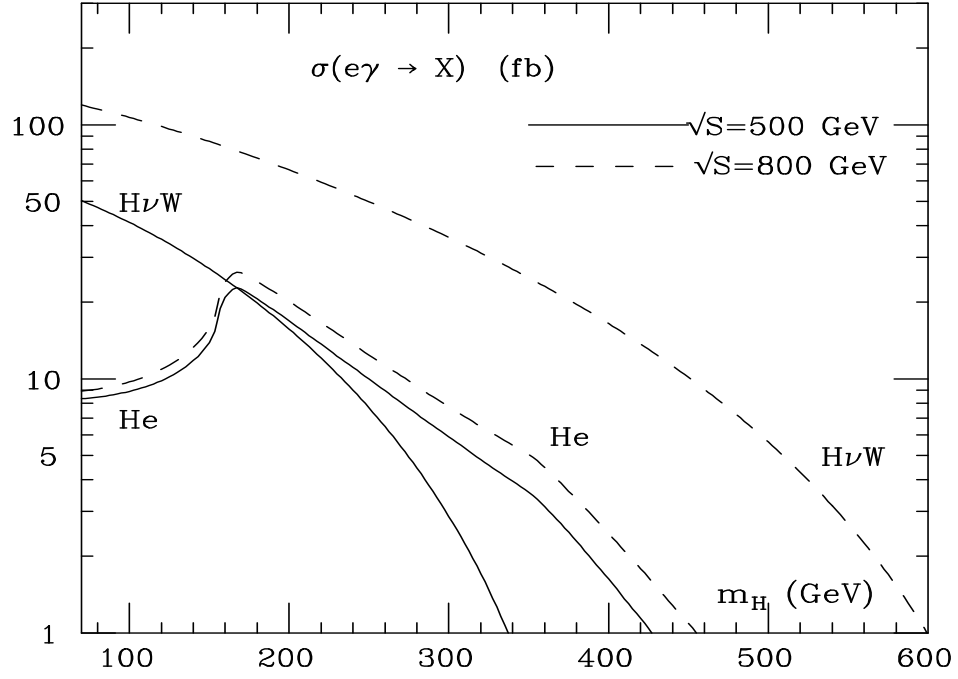


Figure 6: Total cross sections for the two main H production processes.

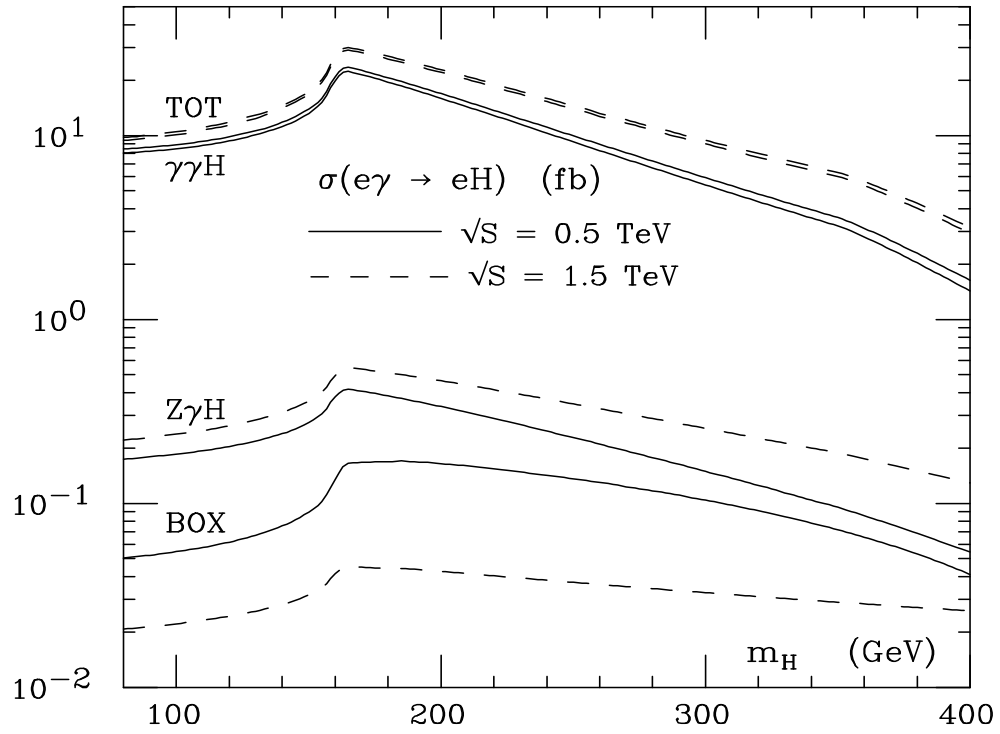


Figure 7: Total cross section for  $e\gamma \rightarrow eH$  plus different partial contributions (see text).

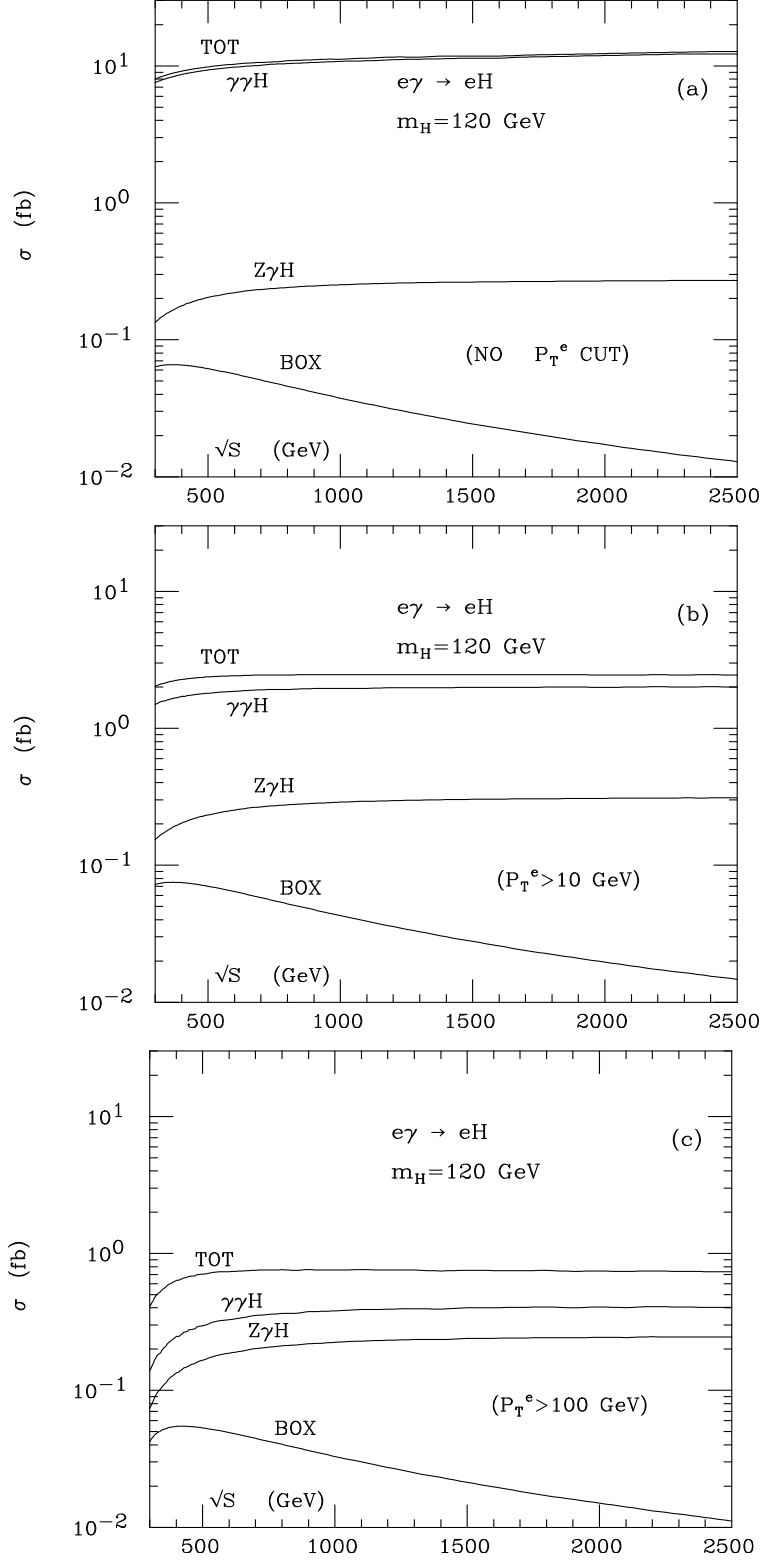


Figure 8: Effect of varying the  $p_T^e$  cut on the  $e\gamma \rightarrow eH$  cross section.

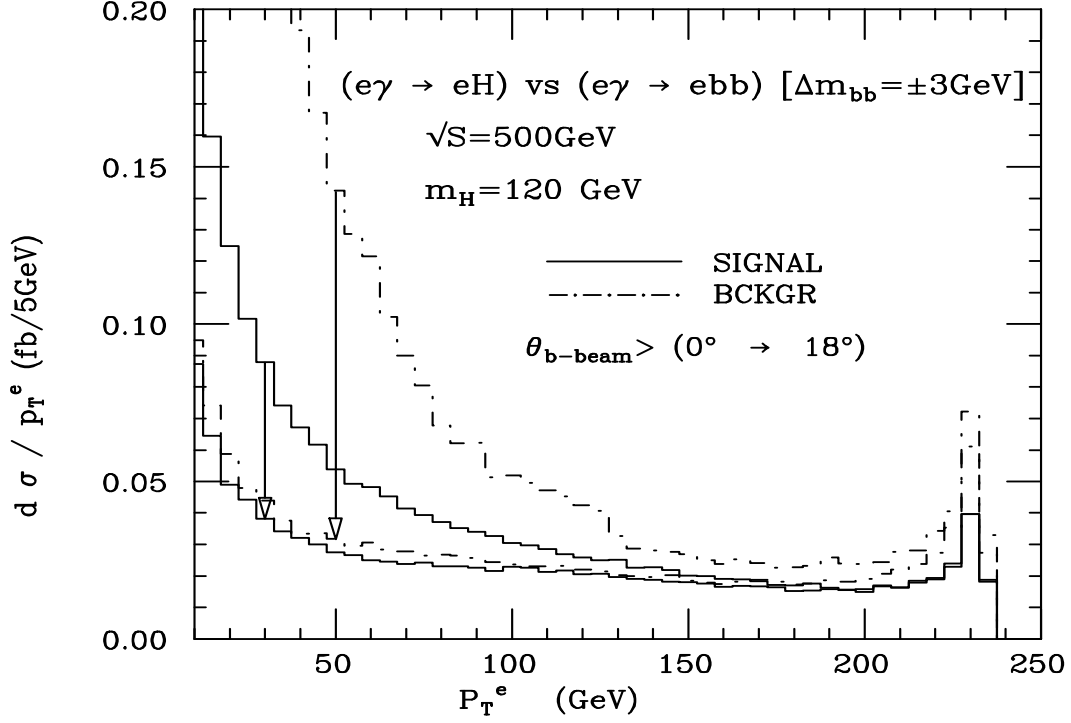


Figure 9: Distribution in  $p_T^e$  for the signal and the background before and after angular cuts on the  $b$ 's is applied.

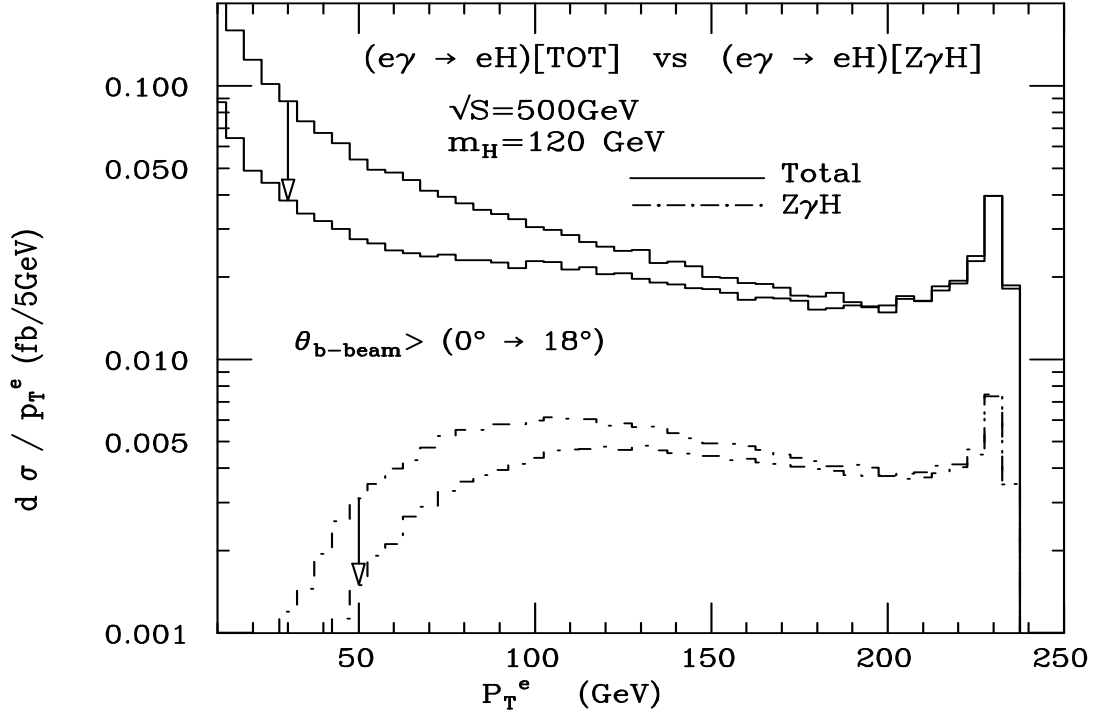


Figure 10: Same as in the previous figure, for the signal and the  $Z\gamma H$  contribution to the signal.



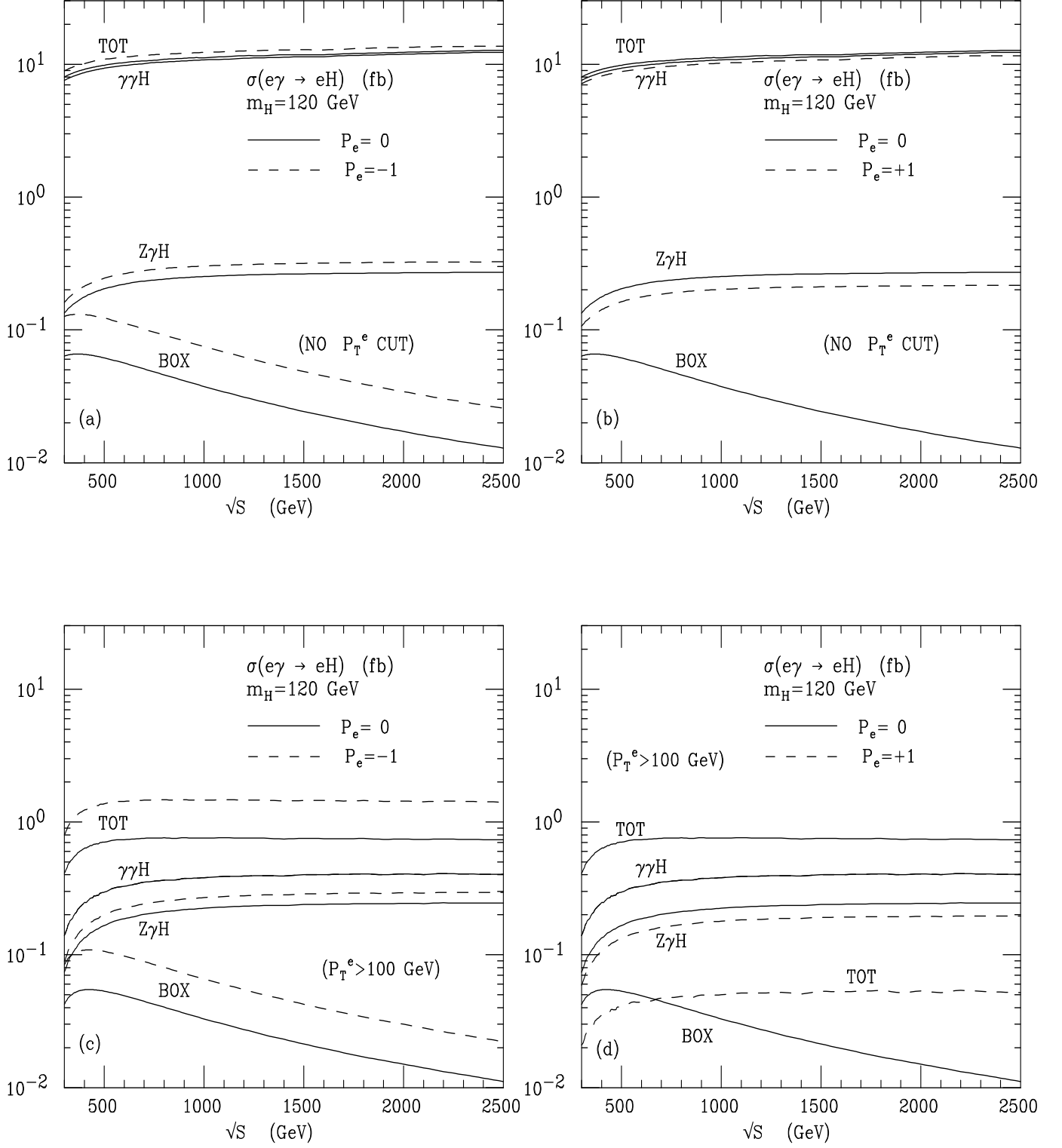


Figure 11: Electron beam polarization effects without [(a) and (b)] and with [(c) and (d)] a cut  $p_T^e > 100$  GeV.

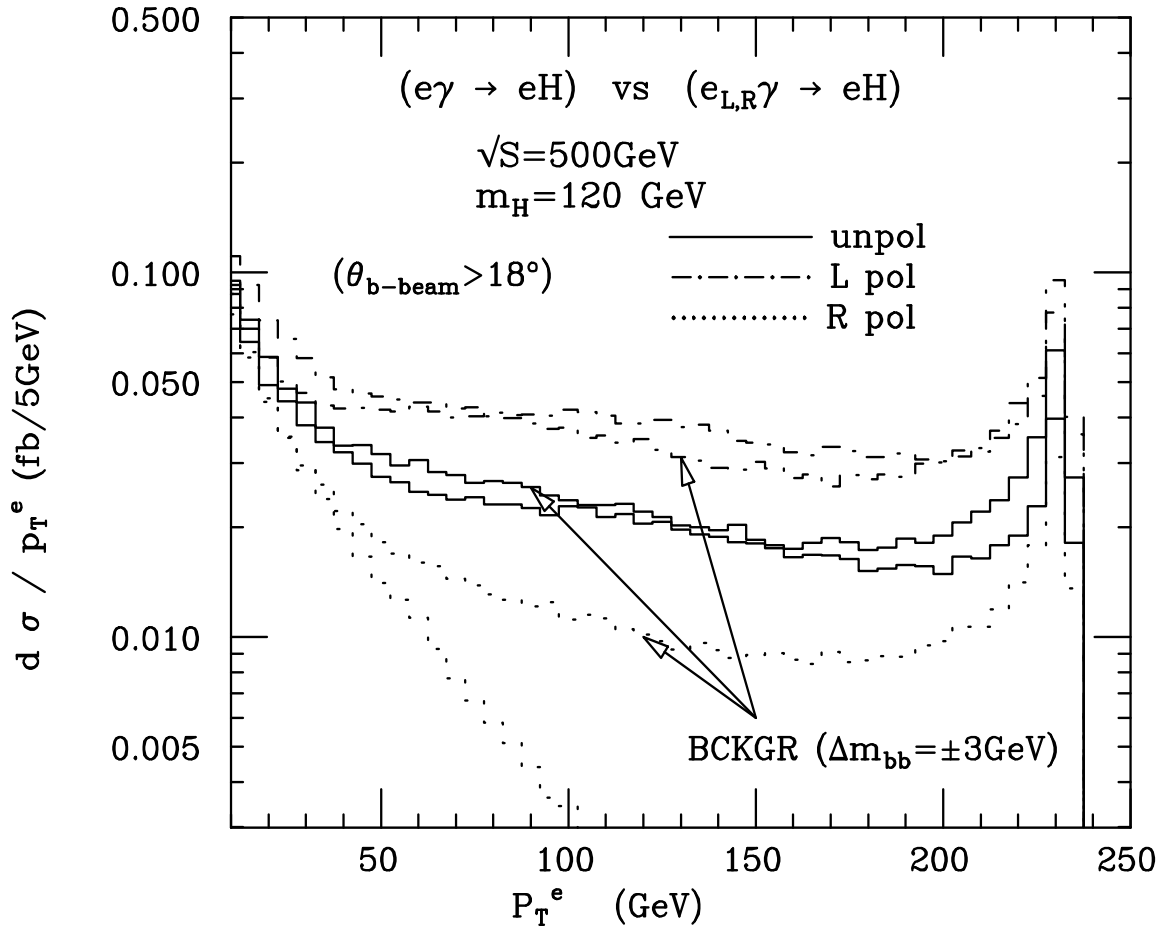


Figure 12: Electron beam polarization effects on the  $p_T^e$  distributions.

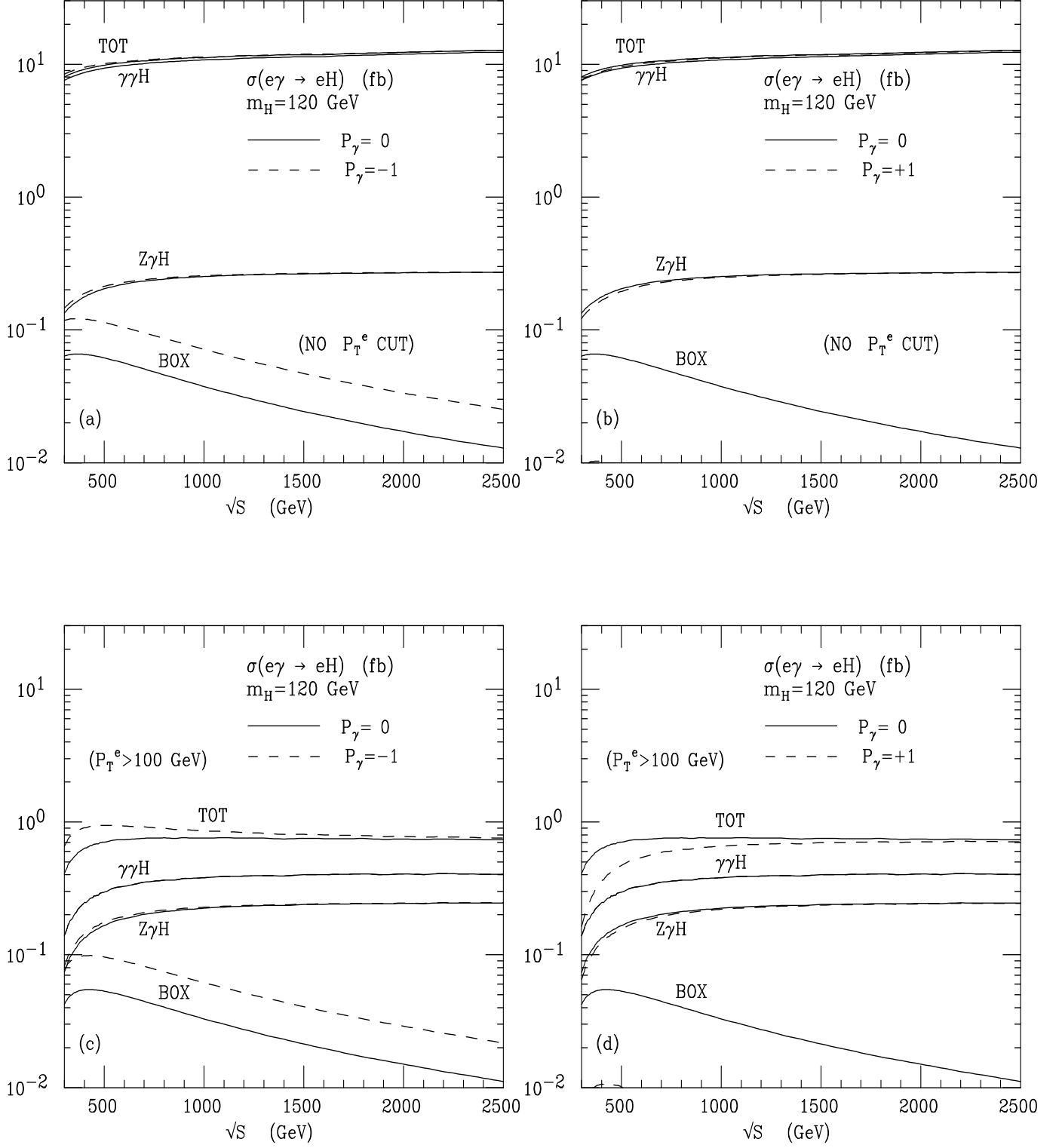


Figure 13: Photon beam polarization effects without [(a) and (b)] and with [(c) and (d)] a cut  $p_T^e > 100 \text{ GeV}$ .

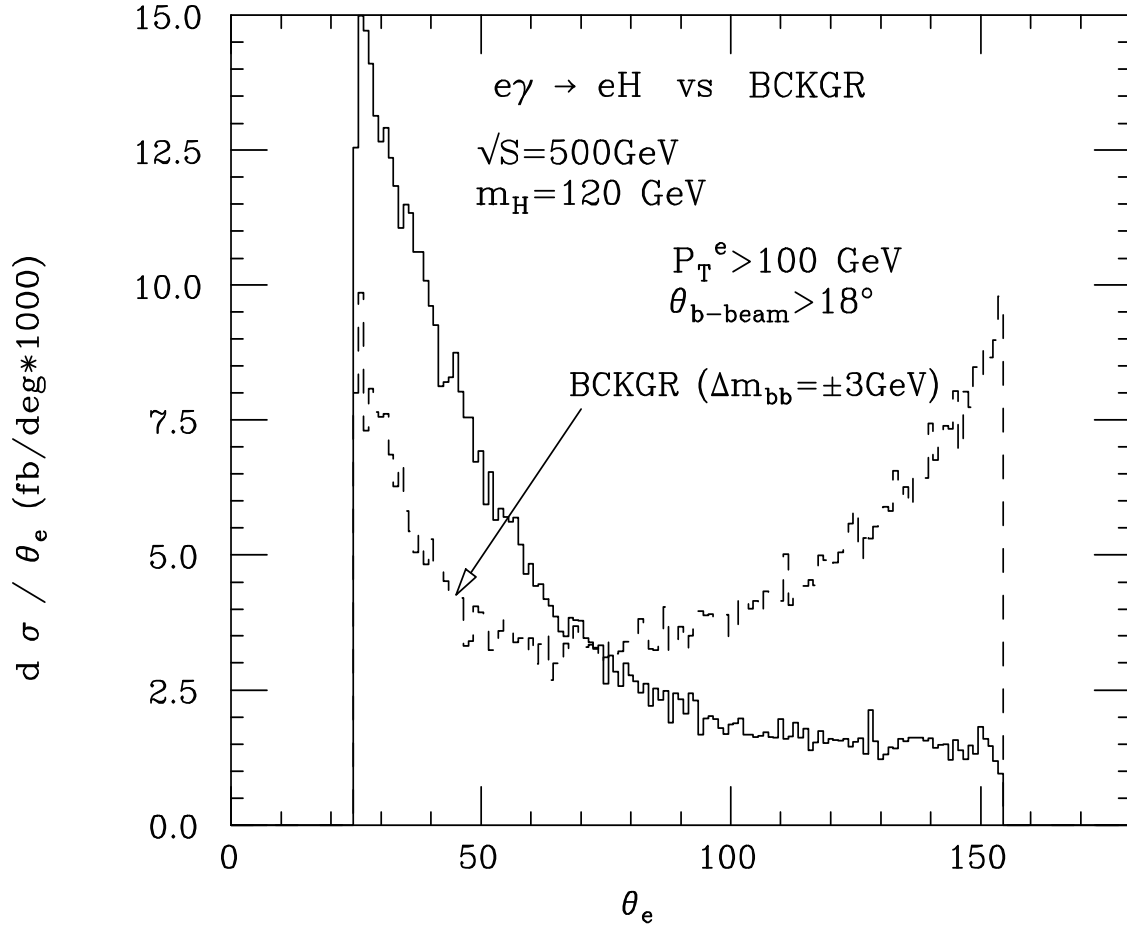


Figure 14: Final electron angular distribution with respect to the initial electron beam. The solid (dashed) line refers to the signal (irreducible  $e\gamma \rightarrow e b \bar{b}$  background). The kinematical cuts applied are shown in the plot. The initial beams are assumed to be unpolarized.